

# Liquid Crystal RESEARCH: CURRENT TRENDS AND FUTURE PERSPECTIVES

GUEST EDITORS: DURGA P. OJHA, HAMIT YURTSEVEN, ASHISH K. PRAJAPATI,  
AND M. L. N. MADHU MOHAN





---

# **Liquid Crystal Research: Current Trends and Future Perspectives**

Advances in Condensed Matter Physics

---

## **Liquid Crystal Research: Current Trends and Future Perspectives**

Guest Editors: Durga P. Ojha, Hamit Yurtseven,  
Ashish K. Prajapati, and M. L. N. Madhu Mohan



---

Copyright © 2013 Hindawi Publishing Corporation. All rights reserved.

This is a special issue published in “Advances in Condensed Matter Physics.” All articles are open access articles distributed under the Creative Commons Attribution License, which permits unrestricted use, distribution, and reproduction in any medium, provided the original work is properly cited.

## Editorial Board

Alexandre Sasha Alexandrov, UK  
Dario Alfe, UK  
Bohdan Andraka, USA  
Daniel Arovas, USA  
Veer Pal Singh Awana, India  
A. Bansil, USA  
Ward Beyermann, USA  
Luis L. Bonilla, Spain  
Mark Bowick, USA  
Gang Cao, USA  
Ashok Chatterjee, India  
R. N. P. Choudhary, India  
Kim Chow, Canada  
Oleg Derzhko, Ukraine  
Gayanath Fernando, USA  
Jörg Fink, Germany  
Yuri Galperin, Norway  
Russell Giannetta, USA

Gabriele F. Giuliani, USA  
James L. Gole, USA  
P. Guptasarma, USA  
Da-Ren Hang, Taiwan  
M. Zahid Hasan, USA  
Yurij Holovatch, Ukraine  
Chia-Ren Hu, USA  
David Huber, USA  
Nigel E. Hussey, UK  
Philippe Jacquod, USA  
Jan Alexander Jung, Canada  
Feo V. Kusmartsev, UK  
Robert Leisure, USA  
Rosa Lukaszew, USA  
Dmitrii Maslov, USA  
Yashowanta N. Mohapatra, India  
Abhijit Mookerjee, India  
Victor V. Moshchalkov, Belgium

Charles Myles, USA  
Vladimir A. Osipov, Russia  
Rolfe Petschek, USA  
S. J. Poon, USA  
Ruslan Prozorov, USA  
Leonid Pryadko, USA  
Charles Rosenblatt, USA  
Mohindar S. Seehra, USA  
Sergei Sergeenkov, Brazil  
Ivan Smalyukh, USA  
Daniel L. Stein, USA  
Michael C. Tringides, USA  
Sergio E. Ulloa, USA  
Attila Virosztek, Hungary  
Markus R. Wagner, Germany  
Gary Wysin, USA  
Gongnan Xie, China  
Fajun Zhang, Germany

## Contents

**Liquid Crystal Research: Current Trends and Future Perspectives**, Durga P. Ojha, Hamit Yurtseven, Ashish K. Prajapati, and M. L. N. Madhu Mohan  
Volume 2013, Article ID 126481, 2 pages

**Dopant Effect and Cell-Configuration-Dependent Dielectric Properties of Nematic Liquid Crystals**, Feng-Ching Lin, Po-Chang Wu, Bo-Ru Jian, and Wei Lee  
Volume 2013, Article ID 271574, 5 pages

**Evanescent Field Enhancement in Liquid Crystal Optical Fibers: A Field Characteristics Based Analysis**, P. K. Choudhury  
Volume 2013, Article ID 504868, 9 pages

**Temperature Dependence of the Tilt Angle for the Smectic A-Smectic C\* Transition in a Mixture of C7-70PDOB Ferroelectric Liquid Crystals near the Tricritical Point**, Mustafa Kurt and Hamit Yurtseven  
Volume 2012, Article ID 201972, 5 pages

**Calculation of the Dielectric Constant as a Function of Temperature Close to the Smectic A-Smectic B Transition in B5 Using the Mean Field Model**, Hamit Yurtseven and Emel Kilit  
Volume 2012, Article ID 262069, 4 pages

**Liquid Crystal Thermography Measurement Uncertainty Analysis and Its Application to Turbulent Heat Transfer Measurements**, Yu Rao and Yamin Xu  
Volume 2012, Article ID 898104, 8 pages

**Applying a Self-Made Automobile Heterodyne Interferometer to Measure the Parameters of Twisted Nematic Liquid Crystal**, Shinn-Fwu Wang, Pei-Cheng Ke, Wesley Lai, Hao Ma, Yi-Zhan Su, and Jyh-Shyan Chiu  
Volume 2012, Article ID 694874, 6 pages

## Editorial

# Liquid Crystal Research: Current Trends and Future Perspectives

**Durga P. Ojha,<sup>1</sup> Hamit Yurtseven,<sup>2</sup> Ashish K. Prajapati,<sup>3</sup> and M. L. N. Madhu Mohan<sup>4</sup>**

<sup>1</sup> School of Physics, Sambalpur University, Jyoti Vihar, Sambalpur, Odisha 768 019, India

<sup>2</sup> Department of Physics, Middle East Technical University, 06531 Ankara, Turkey

<sup>3</sup> Department of Applied Chemistry, Faculty of Technology and Engineering, The Maharaja Sayajirao University of Baroda, Vadodara 390 001, India

<sup>4</sup> Department of Electronics and Communications Engineering, Bannari Amman Institute of Technology, Sathyamangalam 638 401, India

Correspondence should be addressed to Durga P. Ojha; [durga\\_ojha@hotmail.com](mailto:durga_ojha@hotmail.com)

Received 3 September 2013; Accepted 3 September 2013

Copyright © 2013 Durga P. Ojha et al. This is an open access article distributed under the Creative Commons Attribution License, which permits unrestricted use, distribution, and reproduction in any medium, provided the original work is properly cited.

Liquid crystals (LCs) are materials with unique properties mainly due to the presence of partially ordered phases. The ability to form ordered domains is involved in many applications of LCs in electronic devices such as liquid crystal displays (LCDs), spatial modulators, and TV and laptop screens. The occurrence of mesophases in these materials constitutes many challenging research problems. LCs are undergoing a scientific renaissance, both fundamentally and technologically, they have become a pervasive feature of everyday life.

The exploration of these molecular materials is still a challenge since the rapid development of display technology demands new LC materials, which possess as wide a range of properties as possible. The phase structures in these materials involve tricky problems. LCD technology has integrated itself into many facets of our daily lives. They have truly been instrumental in the progression and development of electronic devices. The development and application of materials with well-defined molecular and bulk properties are becoming increasingly important for contemporary technologies. The ability to simulate/synthesize new LC materials with properties and functions far beyond our current reach could lead to meso/nanoscale electronic and mechanical devices that far outstrip our current technological capabilities.

Due to their highly anisotropic constitution, LC materials are quite promising for applications in the field of molecular electronics and optoelectronics. Recently, keeping in pace

with topical science, they have entered into the fascinating domains of space, nanoscience, and technology as well. Even though advances in synthesis and characterization explore many achievements in this regard, it is often desirable to have a sense of material behaviour before it is synthesized. The basic chemical constitution and building blocks of liquid crystal are much helpful, and they act as a model compound to deal with many problems in materials physics and chemistry.

This special issue is aimed at both basic and applied problems, concentrating on four major areas, that is, molecular design, simulation, synthesis, and characterization of liquid crystal materials. The articles in this special issue address some aspects of theoretical formalism and to validate application potentiality of LC compounds. Therefore, it is expected that the research output of the proposed special issue will magnetize a wide variety of research workers from crystallographers, molecular physicists, and biophysicists to structural chemists, organic chemists, polymer chemists, and drug industry, and so forth. This special issue brings together some of the latest developments in this field of liquid crystal research.

## Acknowledgments

We would like to thank all the authors for their excellent contributions to this special issue and all the reviewers for



---

# **Liquid Crystal Research: Current Trends and Future Perspectives**

Advances in Condensed Matter Physics

---

## **Liquid Crystal Research: Current Trends and Future Perspectives**

Guest Editors: Durga P. Ojha, Hamit Yurtseven,  
Ashish K. Prajapati, and M. L. N. Madhu Mohan



---

Copyright © 2013 Hindawi Publishing Corporation. All rights reserved.

This is a special issue published in “Advances in Condensed Matter Physics.” All articles are open access articles distributed under the Creative Commons Attribution License, which permits unrestricted use, distribution, and reproduction in any medium, provided the original work is properly cited.

## Editorial Board

Alexandre Sasha Alexandrov, UK  
Dario Alfe, UK  
Bohdan Andraka, USA  
Daniel Arovas, USA  
Veer Pal Singh Awana, India  
A. Bansil, USA  
Ward Beyermann, USA  
Luis L. Bonilla, Spain  
Mark Bowick, USA  
Gang Cao, USA  
Ashok Chatterjee, India  
R. N. P. Choudhary, India  
Kim Chow, Canada  
Oleg Derzhko, Ukraine  
Gayanath Fernando, USA  
Jörg Fink, Germany  
Yuri Galperin, Norway  
Russell Giannetta, USA

Gabriele F. Giuliani, USA  
James L. Gole, USA  
P. Guptasarma, USA  
Da-Ren Hang, Taiwan  
M. Zahid Hasan, USA  
Yurij Holovatch, Ukraine  
Chia-Ren Hu, USA  
David Huber, USA  
Nigel E. Hussey, UK  
Philippe Jacquod, USA  
Jan Alexander Jung, Canada  
Feo V. Kusmartsev, UK  
Robert Leisure, USA  
Rosa Lukaszew, USA  
Dmitrii Maslov, USA  
Yashowanta N. Mohapatra, India  
Abhijit Mookerjee, India  
Victor V. Moshchalkov, Belgium

Charles Myles, USA  
Vladimir A. Osipov, Russia  
Rolfe Petschek, USA  
S. J. Poon, USA  
Ruslan Prozorov, USA  
Leonid Pryadko, USA  
Charles Rosenblatt, USA  
Mohindar S. Seehra, USA  
Sergei Sergeenkov, Brazil  
Ivan Smalyukh, USA  
Daniel L. Stein, USA  
Michael C. Tringides, USA  
Sergio E. Ulloa, USA  
Attila Virosztek, Hungary  
Markus R. Wagner, Germany  
Gary Wysin, USA  
Gongnan Xie, China  
Fajun Zhang, Germany

## Contents

**Liquid Crystal Research: Current Trends and Future Perspectives**, Durga P. Ojha, Hamit Yurtseven, Ashish K. Prajapati, and M. L. N. Madhu Mohan  
Volume 2013, Article ID 126481, 2 pages

**Dopant Effect and Cell-Configuration-Dependent Dielectric Properties of Nematic Liquid Crystals**, Feng-Ching Lin, Po-Chang Wu, Bo-Ru Jian, and Wei Lee  
Volume 2013, Article ID 271574, 5 pages

**Evanescent Field Enhancement in Liquid Crystal Optical Fibers: A Field Characteristics Based Analysis**, P. K. Choudhury  
Volume 2013, Article ID 504868, 9 pages

**Temperature Dependence of the Tilt Angle for the Smectic A-Smectic C\* Transition in a Mixture of C7-70PDOB Ferroelectric Liquid Crystals near the Tricritical Point**, Mustafa Kurt and Hamit Yurtseven  
Volume 2012, Article ID 201972, 5 pages

**Calculation of the Dielectric Constant as a Function of Temperature Close to the Smectic A-Smectic B Transition in B5 Using the Mean Field Model**, Hamit Yurtseven and Emel Kilit  
Volume 2012, Article ID 262069, 4 pages

**Liquid Crystal Thermography Measurement Uncertainty Analysis and Its Application to Turbulent Heat Transfer Measurements**, Yu Rao and Yamin Xu  
Volume 2012, Article ID 898104, 8 pages

**Applying a Self-Made Automobile Heterodyne Interferometer to Measure the Parameters of Twisted Nematic Liquid Crystal**, Shinn-Fwu Wang, Pei-Cheng Ke, Wesley Lai, Hao Ma, Yi-Zhan Su, and Jyh-Shyan Chiu  
Volume 2012, Article ID 694874, 6 pages

their suggestions and decisive comments. We also expect that the special issue will stimulate the continuing efforts to intensify the liquid crystal research.

*Durga P. Ojha*  
*Hamit Yurtseven*  
*Ashish K. Prajapati*  
*M. L. N. Madhu Mohan*

## Research Article

# Dopant Effect and Cell-Configuration-Dependent Dielectric Properties of Nematic Liquid Crystals

Feng-Ching Lin,<sup>1</sup> Po-Chang Wu,<sup>2</sup> Bo-Ru Jian,<sup>1</sup> and Wei Lee<sup>1,2,3</sup>

<sup>1</sup> Department of Physics, Chung Yuan Christian University, Chung-Li 32023, Taiwan

<sup>2</sup> College of Photonics, National Chiao Tung University, Tainan 71150, Taiwan

<sup>3</sup> Center for Nanotechnology, Chung Yuan Christian University, Chung-Li 32023, Taiwan

Correspondence should be addressed to Wei Lee; [wlee@cycu.edu.tw](mailto:wlee@cycu.edu.tw)

Received 12 July 2012; Revised 7 April 2013; Accepted 17 April 2013

Academic Editor: Hamit Yurtseven

Copyright © 2013 Feng-Ching Lin et al. This is an open access article distributed under the Creative Commons Attribution License, which permits unrestricted use, distribution, and reproduction in any medium, provided the original work is properly cited.

The dielectric polarizations induced by impurity ions in both high- and low-resistivity nematic liquid crystals (NLCs) were investigated. Upon adding carbon nanotubes (CNTs) as a dopant, the former showed no distinct change in the low-frequency ( $< 10^2$  Hz) dielectric spectrum, whereas the latter exhibited dramatic decrease in dielectric constant in that the CNTs remarkably trapped the impurity ions in the NLC of high ionic content. Consequently, the dopant raised the voltage holding ratio by 26% and prolonged the lifetime of the cell. Also investigated were ionic behaviors in the low-resistivity NLC confined in cells with three different configurations. The diffusion constant of the ions in homeotropic cells was found to be the greatest, and the dc conductivity, determined by the diffusion constant, was also higher in the homeotropic ones.

## 1. Introduction

Nematic liquid crystals (NLCs) have ubiquitously been exploited in photonic devices, especially in current flat panel displays. Regardless of their origins, impurity ions existing in liquid-crystal (LC) cells have long been a nuisance to the global LC display (LCD) industry. It is well known that the cumulative impurity ions produce an internal, counteracting electric field in an LC cell under voltage application, causing many problems such as the reduction of voltage holding ratio, increase in threshold voltage, image sticking, gray-level shift, image flickering, and the slow-down of switching response [1–4]. In order to solve these issues, some research groups have adopted a postsynthetic approach [5] and demonstrated that doping an adequate amount of carbon nanotubes (CNTs) into NLCs can help suppress the unwanted field-screening effect [6]. The fact that the impurity ions can be effectively trapped by CNTs via charge transfer substantially improves the electrooptical performance of an LC device [7, 8]. With a compatible shape to the rodlike molecules of NLCs, tubular CNTs are known as a one-dimensional nanomaterial, possessing

unique material characteristics to be promisingly applied in modern photonic and semiconductor devices. As a matter of fact, recent laboratory studies have demonstrated their potential for flat panel display applications, permitting their roles in electrodes, thin-film transistors, alignment layers, and field-emission devices.

The quality of an LC material for photonic applications can be examined by low-frequency dielectric spectroscopy [9]. It has been established that the LC dielectric behavior at low frequencies is dictated by the charge carrier transport process and is susceptible to the material properties of the alignment layers if any [10]. Interestingly but not surprisingly, Costa et al. revealed that impurity ions in the NLC E7 travel to electrodes faster in homeotropic cells than in homogeneous cells due to the anisotropy in diffusion constant [11]. Thus, the underlying mechanisms depend upon the materials used and the properties of the cell.

In this comparative study we used a low-resistivity NLC (E7) and a high-resistivity NLC (CYLC-01) to observe their low-frequency polarizations contributed by mobile ions. The dielectric spectra of the two eutectic NLC materials were compared between 10 Hz and 10 kHz. The dopant effects

of CNTs on the dielectric properties of the two NLCs were investigated. In addition, by expanding the frequency range to  $10^{-1}$ – $10^4$  Hz, the ionic transport behaviors were analyzed for three distinctive (homogeneous, twisted-nematic, and homeotropic) cell configurations for the ion-rich NLC E7.

## 2. Experimental

Both low- and high-resistivity NLC materials were employed for comparison; they were E7 and CYLC-01, respectively. With a typical bulk resistivity of  $\sim 10^{11}$   $\Omega$ -cm, E7 is a well-known commercial eutectic mixture (from Merck), consisting of primarily 4'-*n*-pentyl-4-cyanobiphenyl and three other cyano compounds. Owing to its high polarity, E7 exhibits a strong permanent dipole moment along the molecular axis, possesses large dielectric anisotropy ( $\Delta\epsilon' \sim 14$  at 1 kHz and 20°C [12]), and is notorious for its vulnerability to ionic contamination. On the other hand, the mixture CYLC-01 is an ultrapure CF<sub>2</sub>O-based TFT-grade NLC. Its excellent material quality, including high bulk resistivity of  $\sim 10^{14}$   $\Omega$ -cm, allows its appearance in the modern active-matrix LC displays. Both the LC substances are of positive dielectric anisotropy (defined as the difference between the parallel component  $\epsilon_{\parallel}$  and perpendicular component  $\epsilon_{\perp}$  of the real dielectric constant). The dopant material used was ultrapure multiwalled carbon nanotubes (CNTs) with inner diameters of 2-3 nm and  $\sim 21$  graphene layers (from SRS Research). According to our prior experience, the optimal CNT concentration of 0.05 wt% was adopted [13]. Four material samples were prepared, including pure E7, E7/CNT, pure CYLC-01, and CYLC-01/CNT, which were individually injected into empty homogeneous-alignment cells by capillary action in the isotropic phase. The cell gap was 11.3  $\mu\text{m}$  between the conducting glass substrates, and the effective electrode area was 1  $\text{cm}^2$ . For the second part of the experiment concerning the influence of cell configuration, we prepared five pristine E7 samples for each type of cell structure. The cell configurations investigated in this work included the homogeneous (i.e., planar alignment), 90° twisted-nematic, and homeotropic (i.e., vertical alignment) structures. The alignment layers for the 6.2  $\mu\text{m}$  thick homogeneous and twisted cells were the same polyimide (Nissan SE-2170). The homeotropic cells of  $\sim 5$   $\mu\text{m}$  in thickness were purchased from EHC, Japan, and the aligning material is unknown.

The complex dielectric constant was acquired with an LCR meter (HIOKI 3522-50 LCR HiTESTER) having capability of measurement in the frequency range from 1 mHz to 100 kHz and basic measurement accuracy of  $\pm 0.08\%$ . The probe voltage adopted in this study was 50 mV<sub>rms</sub> in the sinusoidal waveform, which was much smaller than the LC threshold voltage. The voltage holding ratio (VHR) experiment [14] was carried out to simulate the charging and discharging properties of E7 cells, by which the cell performance of the doped one was examined. The temperatures for the first part and second part of the experiment were 303 K and 296 K, respectively.

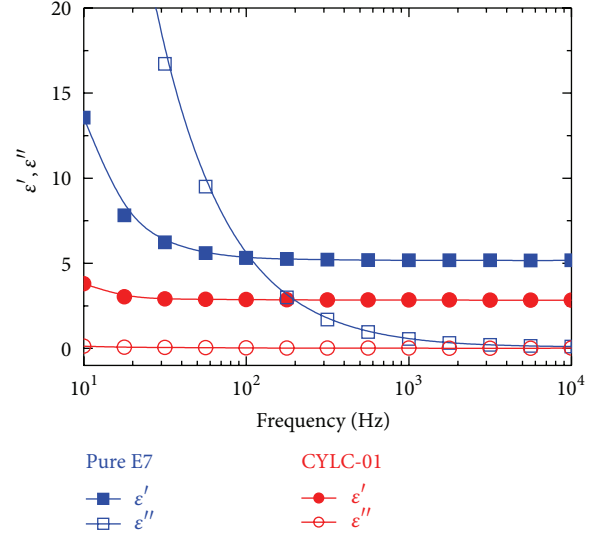


FIGURE 1: The dielectric spectra of the low-resistivity NLC E7 and high-resistivity NLC CYLC-01 confined in homogeneous cells at 303 K.  $\epsilon'$  and  $\epsilon''$  are the real and imaginary parts of the complex dielectric function.

## 3. Results and Discussion

Figure 1 shows the frequency dependence of the real and imaginary parts of the complex dielectric function ( $\epsilon' - i\epsilon''$ ) of pure E7 and pure CYLC-01. In the low-frequency region ( $f < 10^2$  Hz), the dielectric behavior was attributable to the space-charge polarization. Both frequency-varying  $\epsilon'$  and  $\epsilon''$ , dominated by the ionic effect in this frequency region, are proportional to  $f^{-3/2}$  and  $f^{-1}$ , respectively. Taking the diffusive motion of the impurity ions into account, the expressions for the ionic contributions to the dielectric dispersion  $\epsilon'$  and dielectric loss  $\epsilon''$  in the appropriate frequency range in the nematic LC cell are [15]

$$\epsilon'(f) = \frac{nq^2 D^{3/2}}{\pi^{3/2} \epsilon_0 L k_B T} f^{-3/2} + \epsilon'_b, \quad (1)$$

$$\epsilon''(f) = \frac{nq^2 D}{\pi \epsilon_0 k_B T} f^{-1}, \quad (2)$$

respectively, where  $n$  is the mobile ion concentration,  $q$  is the charge of an ion,  $D$  is the diffusion constant of the ion,  $L$  is the thickness of the cells,  $\epsilon_0$  is the permittivity in free space,  $k_B$  is the Boltzmann constant,  $T$  is the absolute temperature, and  $\epsilon'_b$  is the intrinsic dielectric constant of the NLC bulk. The ionic contribution decreased with increasing frequency. At low frequencies the impurity ions had enough time to reach the electrodes to form dipole moments, while at high frequencies the space-charge polarization could not keep up with the polarity alteration of the electric field, which, in turn, led to the dielectric relaxation. The constant value of  $\epsilon'$  between  $10^3$  and  $10^4$  Hz was mainly contributed by the intrinsic LC dielectric term  $\epsilon'_b$ . It is clear from Figure 1 that the dielectric relaxation in the low-frequency region ( $10 \text{ Hz} < f < 100 \text{ Hz}$ ) was not evident in the dielectric spectrum

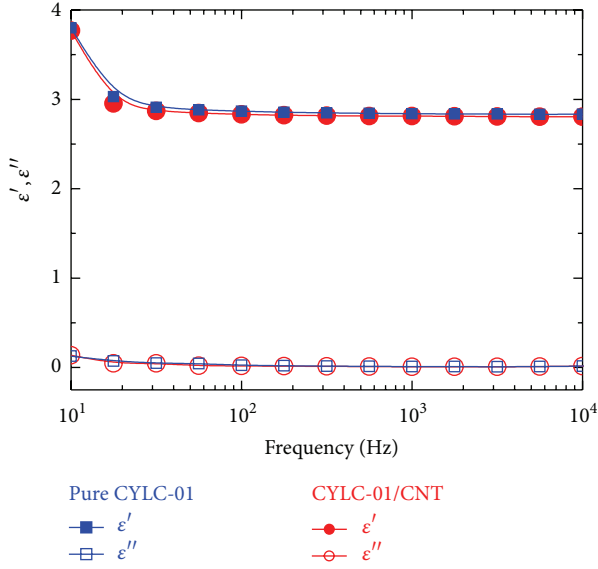


FIGURE 2: The dielectric spectra of pristine and 0.05 wt% CNT-doped CYLC-01 in homogeneously aligned cells at 303 K.

of the superfluorinated LC mixture CYLC-01. As mentioned above, CYLC-01 was a high-resistivity NLC, connoting that it contained a very limited amount of impurity ions. Consequently, the ionic contribution was not as significant at low frequencies compared with the E7 counterpart.

Figure 2 depicts the dielectric spectra of pure as well as CNT-doped CYLC-01 samples. Since their real parts almost coincide with each other and imaginary parts are virtually identical, the dopant effect on the dielectric behavior (in the frequency range studied) was trivial in the TFT-grade NLC. In contrast, the impact of the dopant on the low-frequency dielectric spectrum was very pronounced for the E7 host as shown in Figure 3. One can see from this figure that, after doping 0.05-wt% CNTs in E7, the dielectric permittivity ( $\epsilon'$ ) decreased in the low-frequency region and the relaxation frequency shifted to the lower frequency. Again, E7 is a low-resistivity NLC, which contains a large amount of impurity ions. The CNTs as an additive in the ion-rich nematic host effectively trapped mobile ions [5] to give rise to the reduction in space-charge polarization.

The VHR is an important measure of the LCD performance. It is conventionally defined as

$$\text{VHR} (\%) = \frac{V_t}{V_i} \times 100\%, \quad (3)$$

where  $V_i$  is the initial (or input) pulse voltage (5 V in this study) and  $V_t$  is the terminal voltage of the LC cell during a frame time of 16.67 ms. One can see from Figure 4 that, by adding an adequate amount of CNTs in E7, the VHR was promoted from 48% to 61%, yielding a substantial increase by 26%. In order to monitor the degradation of the cell manifested by the decrease in VHR over time, a four-day observation was made. Figure 5 illustrates the time-evolved VHR curves for the doped and undoped cells. The monotonic fall of the VHR in both cells can be explained by the ascending

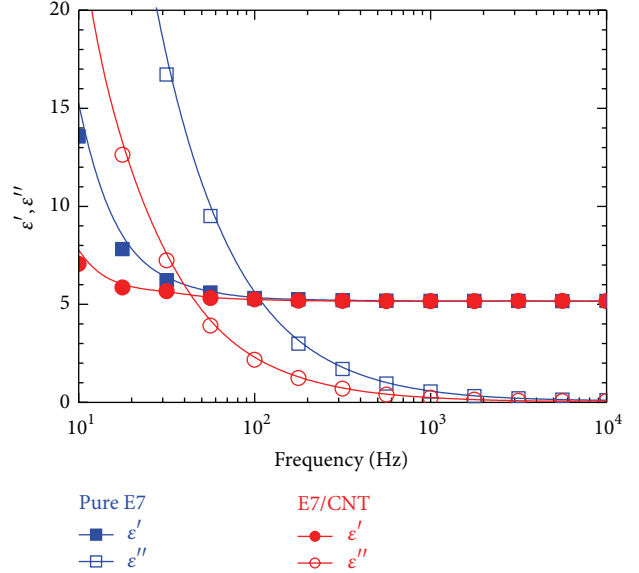


FIGURE 3: The dielectric spectra of pure and 0.05 wt% CNT-doped E7 in homogeneous cells at 303 K.

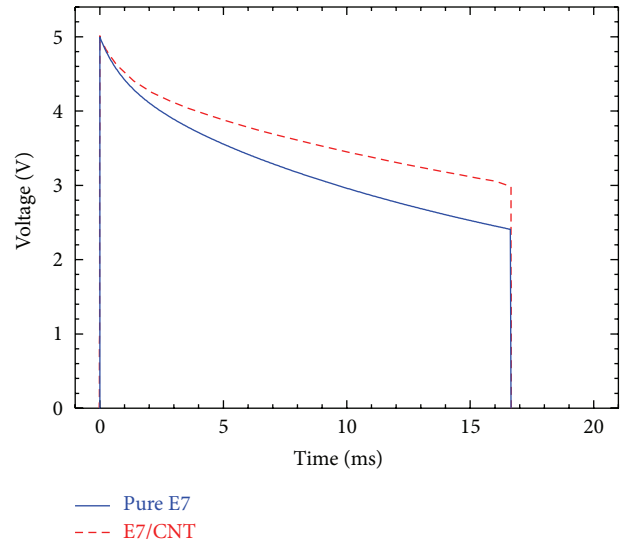


FIGURE 4: Voltage responses of doped and undoped E7 cells to a 5-V square-wave pulse of 15.6  $\mu\text{s}$ .

ionic concentration after the cell fabrication [16]. Using the monoexponential decay expression  $\text{VHR}(t) = Ae^{-t/\tau}$ , where  $A$  is the VHR at time  $t = 0$  and  $\tau$  is the characteristic lifetime, one can fit the experimental data and obtain a lifetime of 118 h for the doped cell compared with that of 59 h for the undoped counterpart. Obviously, the addition of CNTs in E7 prolonged the cell lifetime before degradation.

Figure 6 shows the dielectric spectra of E7 in various cells with homogeneous, twisted, and homeotropic alignment. In the  $10^3$ – $10^4$  Hz frequency region, the dielectric constant  $\epsilon'$  of E7 was the largest in the homeotropic configuration, because

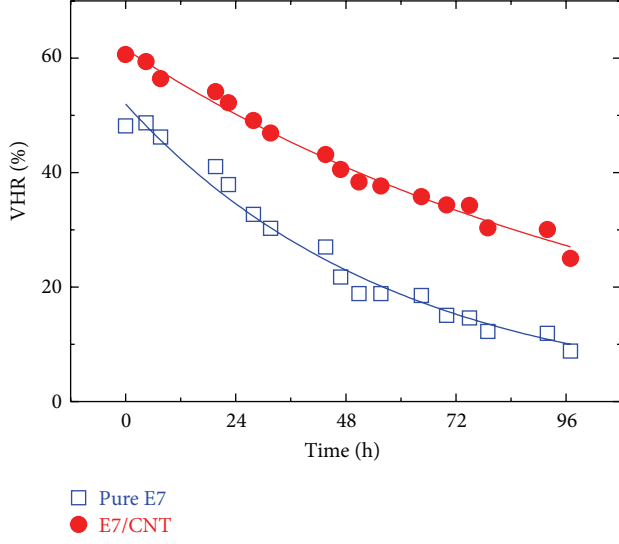


FIGURE 5: Time-evolved VHR curves in a period of 96 h.

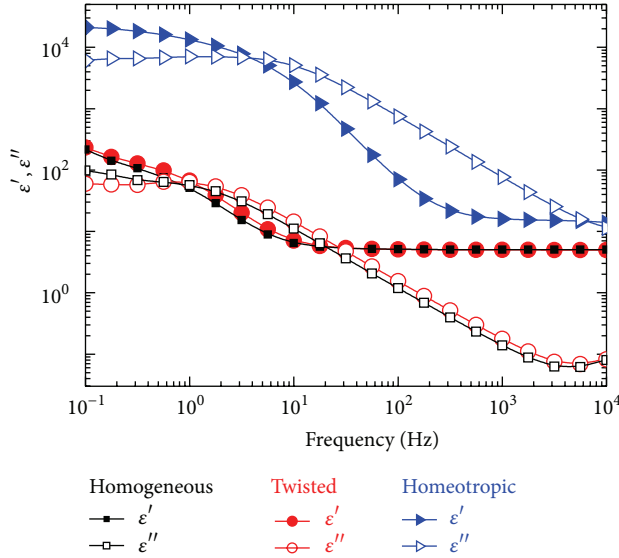


FIGURE 6: The dielectric spectra of E7 in homogeneous, twisted, and homeotropic cells at 296 K.

E7 possessed positive dielectric anisotropy. Note that the effective dielectric constant  $\epsilon$  can be expressed by [17]

$$\epsilon = \epsilon_{\perp} + \Delta\epsilon \sin^2\theta, \quad (4)$$

where  $\theta$  is the tilt angle between the substrate plane and the LC director. Thus, the complex dielectric constant measured in a homeotropic cell is the sole contribution of the parallel component  $\epsilon_{\parallel}$ . In the frequency region of  $f < 10^3$  Hz, both  $\epsilon'$  and  $\epsilon''$  functions can be individually fitted by (1) and (2), respectively, for calculation of their ion density  $n$  and diffusion constant  $D$ . The results are listed in Table 1.

The impurity ions in the LC bulk can be contributed by the dissociation of the LC material itself and ion injection from the alignment or electrode layer [18, 19]. Based on

TABLE 1: Ion concentration  $n$  and diffusion constant  $D$  in E7 for homogeneous, twisted, and homeotropic cells at 296 K.

Cell type	$n$ (cm <sup>-3</sup> )	$D$ (cm <sup>2</sup> s <sup>-1</sup> )
Homogeneous	$1.80 \times 10^{13}$	$2.67 \times 10^{-7}$
Twisted	$1.74 \times 10^{13}$	$3.55 \times 10^{-7}$
Homeotropic	$5.12 \times 10^{15}$	$5.72 \times 10^{-7}$

the data displayed in Table 1, the ion concentration in the homeotropic cells was much (two orders of magnitude) higher than that in the other cells with different configurations. Here, the most likely explanation is the occurrence of ion injection into the LC bulk from the homeotropic alignment layers because the electrodes are identical. The ionic concentrations in the homogeneous and twisted-nematic cells are quite the same due to the use of the same aligning material.

The diffusion constant  $D$  is anisotropic and related to the viscosity and electrical conductivity of the medium [7, 11]. Table 1 reveals that  $D$  in a homeotropic cell was larger in comparison with that in a homogeneous one. This result, arising from the fact that the diffusion constant along the molecular axis is greater (namely,  $D_{\parallel} > D_{\perp}$ ), is in good agreement with an earlier study by Costa et al. [11]. We also observed that  $D$  in the twisted cells is somewhat larger than that in the homogeneous cells. Since the viscosity of the LC E7 in splay and twist molecular configurations is identical [20], we believe that the difference can be ignored due to the experimental error and uncertainties in the curve-fitting process. As a result, it can be summarized that the alignment layer and molecular orientation play an important role in ionic concentration and diffusion constant, respectively. The dc conductivity can be written as

$$\sigma_{dc} = qn\mu, \quad (5)$$

where  $\mu$  is the ion mobility. According to the Einstein relation

$$\mu = \frac{q}{k_B T} D, \quad (6)$$

(5) becomes

$$\sigma_{dc} = \frac{nq^2 D}{k_B T}, \quad (7)$$

indicating that the ionic dc conductivity  $\sigma_{dc}$  is not only proportional to the ion concentration  $n$ , but also to the diffusion constant  $D$ . Thus, the conductivity of an LC cell changes with the variation of  $D$  in different LC alignment.

## 4. Conclusions

This paper presents the low-frequency ( $f < 10^2$  Hz) dielectric behaviors induced by impurity ions in LC cells under different conditions. In the high-resistivity NLC (CYLC-01) which contained a low concentration of impurity ions, we did not observe an evident sign of the mobile-ion polarization and the dielectric constant did not seem to change after doping

CNTs. By contrast, the dielectric relaxation was obviously observed in the low-resistivity NLC (E7) rich in impurity ions. Our experimental results suggested that CNTs as a dopant can effectively suppress the ion effect in the low-resistivity NLC, thereby promoting the VHR substantially. In addition, the low-resistivity NLC confined in homeotropic cells, in comparison with cells in the homogeneous and twisted configurations, exhibited the highest impurity-ion concentration, implying significant ion injection from the corresponding alignment layers.

## Acknowledgment

The authors are thankful for the financial support of the National Science Council of Taiwan under Grant nos. NSC 98-2112-M-033-004-MY3, NSC 101-2112-M-009-018-MY3, and NSC 101-2811-M-009-059.

## References

- [1] S. H. Perlmutter, D. Doroski, and G. Moddel, "Degradation of liquid crystal device performance due to selective adsorption of ions," *Applied Physics Letters*, vol. 69, no. 9, pp. 1182–1184, 1996.
- [2] C. Colpaert, B. Maximus, and A. de Meyere, "Adequate measuring techniques for ions in liquid crystal layers," *Liquid Crystals*, vol. 21, no. 1, pp. 133–142, 1996.
- [3] V. A. Tsevetkov and O. V. Tevetkov, "Ions influence on electrooptical characteristics of NLC," *Molecular Crystals and Liquid Crystals*, vol. 368, no. 1, pp. 625–632, 2001.
- [4] L. O. Palomares, J. A. Reyes, and G. Barbero, "Optical response of a nematic sample submitted to a periodic external electric field: role of the ionic impurities," *Physics Letters A*, vol. 333, no. 1-2, pp. 157–163, 2004.
- [5] M. Rahman and W. Lee, "Scientific duo of carbon nanotubes and nematic liquid crystals," *Journal of Physics D*, vol. 42, Article ID 063001, 12 pages, 2009.
- [6] H. Y. Chen and W. Lee, "Suppression of field screening in nematic liquid crystals by carbon nanotubes," *Applied Physics Letters*, vol. 88, Article ID 222105, 3 pages, 2006.
- [7] B. R. Jian, C. Y. Tang, and W. Lee, "Temperature-dependent electrical properties of dilute suspensions of carbon nanotubes in nematic liquid crystals," *Carbon*, vol. 49, no. 3, pp. 910–914, 2011.
- [8] H. H. Liu and W. Lee, "Ionic properties of liquid crystals dispersed with carbon nanotubes and montmorillonite nanoplatelets," *Applied Physics Letters*, vol. 97, no. 17, Article ID 173501, 3 pages, 2010.
- [9] C. Y. Tang, S. M. Huang, and W. Lee, "Electrical properties of nematic liquid crystals doped with anatase TiO<sub>2</sub> nanoparticles," *Journal of Physics D*, vol. 44, Article ID 355102, 5 pages, 2011.
- [10] S. Murakami and H. Naito, "Electrode and interface polarizations in nematic liquid crystal cells," *Japanese Journal of Applied Physics*, vol. 36, no. 4, pp. 2222–2227, 1997.
- [11] M. R. Costa, R. A. C. Altafim, and A. P. Mamma, "Ionic impurities in nematic liquid crystal displays," *Liquid Crystals*, vol. 28, no. 12, pp. 1779–1783, 2001.
- [12] Merck data sheets.
- [13] H. Y. Chen, W. Lee, and N. A. Clark, "Faster electro-optical response characteristics of a carbon-nanotubenematic suspension," *Applied Physics Letters*, vol. 90, Article ID 033510, 3 pages, 2007.
- [14] C. Y. Tang, Y. C. Lin, and W. Lee, "Voltage holding ratio of a nematic liquid crystal cell under UV exposure," in *Proceedings of the Photonics Global Conference*, Suntec Singapore International Convention & Exhibition Centre, Singapore, December 2010.
- [15] G. Barbero and A. L. Alexe-Ionescu, "Role of the diffuse layer of the ionic charge on the impedance spectroscopy of a cell of liquid," *Liquid Crystals*, vol. 32, no. 7, pp. 943–949, 2005.
- [16] H. H. Liu and W. Lee, "Time-varying ionic properties of a liquid-crystal cell," *Applied Physics Letters*, vol. 97, Article ID 023510, 3 pages, 2010.
- [17] W. Lee, J. S. Gau, and H. Y. Chen, "Electro-optical properties of planar nematic cells impregnated with carbon nanosolids," *Applied Physics B*, vol. 81, no. 2-3, pp. 171–175, 2005.
- [18] S. Murakami and H. Naito, "Charge injection and generation in nematic liquid crystal cells," *Japanese Journal of Applied Physics*, vol. 36, no. 2, pp. 773–776, 1997.
- [19] H. de Vleeschouwer, A. Verschuere, F. Bougrioua et al., "Dispersive ion generation in nematic liquid crystal displays," *Japanese Journal of Applied Physics A*, vol. 41, no. 3, pp. 1489–1494, 2002.
- [20] H. J. Coles and M. S. Bancroft, "Viscosity coefficients and elastic constants of nematic solutions of a side-chain polymer," *Molecular Crystals and Liquid Crystals Science and Technology. Section A*, vol. 237, no. 1, pp. 97–110, 1993.

## Research Article

# Evanescent Field Enhancement in Liquid Crystal Optical Fibers: A Field Characteristics Based Analysis

**P. K. Choudhury**

*Institute of Microengineering and Nanoelectronics (IMEN), Universiti Kebangsaan Malaysia (UKM), 43600 Bangi, Selangor, Malaysia*

Correspondence should be addressed to P. K. Choudhury; [pankaj@ukm.my](mailto:pankaj@ukm.my)

Received 11 July 2012; Accepted 6 February 2013

Academic Editor: Durga Ojha

Copyright © 2013 P. K. Choudhury. This is an open access article distributed under the Creative Commons Attribution License, which permits unrestricted use, distribution, and reproduction in any medium, provided the original work is properly cited.

The paper presents the analysis of the electromagnetic wave propagation through liquid crystal optical fibers (LCOFs) of two different types—conventional guides loaded with liquid crystals (addressed as LCOFs) and those with additional twists due to conducting helical windings (addressed as HCLCOFs). More precisely, the three-layer optical waveguide structures are considered along with its outermost region being loaded with radially anisotropic liquid crystal material and the inner regions being made of usual silica, as used in conventional optical fibers. In addition to that, LCOF with twists introduced in the form of conducting helical windings at the interface of the silica core and the liquid crystal clad is also taken into account. Emphasis has been put on the power confinements by the lower-order TE modes sustained in the different sections of the LCOF structure. The results demonstrate useful applications of these guides in integrated optics as the power sustained in the liquid crystal section by the excited TE modes remains very high. In the case of twisted clad liquid crystal guides, descriptions are limited to the nature of dispersion relation only under the TE mode excitation, and corresponding to the cases of helix orientations being parallel and perpendicular to the optical axis.

## 1. Introduction

Optical fibers are of immense use in communication technology, which may be either for the long distance use, for example telecommunication needs, or the short distance ones, for example sensing and so forth. In either case, optical fibers can be designed to act as active and/or passive device. The propagation characteristics of various types of optical fibers have been discussed in the literature. In this respect, the fiber itself may either have wide varieties of geometries ranging from conventional to the unconventional ones, or the guide may possess different forms of material compositions. The characteristics of electromagnetic wave propagation through optical fibers are greatly dependent on the type of material which the guide is composed of.

Among the others, fibers made of liquid crystals [1–3] fall into the category of complex mediums and proved to be greatly attractive for multifarious applications [4, 5] because these materials present the distinct characteristic of anisotropic nature in their physical properties [6, 7]. Investigators have reported liquid crystal optical fibers (LCOFs)

of different forms of constructions in respect of geometry as well as material distributions. LCOFs may consist of liquid crystals either in the core [8–10] or in the clad section [9–11] of the guide. High optical anisotropy of liquid crystals makes them as demanding smart materials for their usage in a wide range of applications in the area of integrated optics [7, 12]. These can be used in electric field sensing as the macroscopic optical properties of liquid crystals can be altered under the influence of external electrical field [13]. Yoshino et al. [14] demonstrated the use of LCOFs in electric field sensing based on the inherent property of liquid crystals that these exhibit the largest electrooptic effect among known materials. In all the aforesaid applications, the clad region of the guide consists of liquid crystal. For the fabrication of directional couplers, LCOFs are used with the liquid crystal section sandwiched between two side polished fibers, and coaxial fibers are embedded in liquid crystals.

Applications of liquid crystals make it clear that these exhibit distinct feature of polarization anisotropy which may have two different directions of orientation—radial and azimuthal anisotropies; the latter one is less discussed in

the literature. In the present paper, we consider the nematic form of liquid crystals along with its radially anisotropic nature to constitute the fiber clad, the core region being made of standard silica. In forming such LCOFs, the radial anisotropy of liquid crystal can be obtained by capillary action after inserting the liquid crystal section (of the fiber) into a capillary tube coated with N,N-dimethyl-N-octadecyl-3-aminopropyltrimethoxysilyl chloride [11].

Considering the importance of the usage of liquid crystals in optical fibers, such guides with tapered structures have been discussed before [15]. Since the propagation of power through a guide plays the determining role for specific applications of the guide, the scope of the present paper lies in the analysis of LCOFs in respect of power confinement factor. We consider a three-layer LCOF, of which the outermost clad is made of radially anisotropic liquid crystal material, and determine the power propagation characteristics corresponding to two lower-order TE modes in the guides of different dimensions. It has been observed that the TE modes transport relatively high amount of power through the liquid crystal clad. These interesting features of radially anisotropic LCOFs indicate their usefulness in the fabrication of different coupling devices used in the area of integrated optics, and also, in optical sensing where the method of evanescent field absorption is primarily implemented.

The investigations are extended to the case of LCOFs with conducting helical windings (i.e., HCLCOFs—the helical clad liquid crystal optical fibers) introduced at the core-clad interface of the guide. In such fibers, the angle of pitch (of the helix in use) exhibits dominant characteristics to alter the wave propagation, and the working principles are based on the theory of low- and medium-power travelling wave tubes (TWTs) [16]. Implementing the concept in the case of dielectric optical fibers, studies have appeared in the literature for fibers having circular and elliptical cross-sections [17–20]. However, in the present paper, as stated before, the existence of the liquid crystal layer will modify the propagation characteristics. The dispersion relation for such types of guides (i.e. HCLCOFs) is deduced, and the features are reported corresponding to the cases of helical turns being parallel as well as perpendicular to the optical axis.

## 2. The Analytical Approach

**2.1. The Case of LCOFs.** Figure 1 illustrates the cross-sectional view of the three-layer LCOF, of which the (infinitely extended) outermost clad is made of radially anisotropic liquid crystal material; the core and the inner clad regions being constructed of linear, homogeneous, and isotropic dielectrics having the refractive index (RI) values as  $n_1$  and  $n_2$  ( $n_1 > n_2$ ). Also,  $n_o$  and  $n_e$ , respectively, are the ordinary and the extraordinary RIs of the liquid crystal section. Further,  $\rho_1$  and  $\rho_2$  are, respectively, the radii of the core and the inner clad regions. The dashed lines in the radial direction (in Figure 1) indicate the radial orientation of liquid crystal molecules. We consider the time harmonic waves with angular frequency  $\omega$  (in the unbounded medium) propagate along the  $z$ -direction with the propagation constant  $\beta$ , and the wave is harmonic

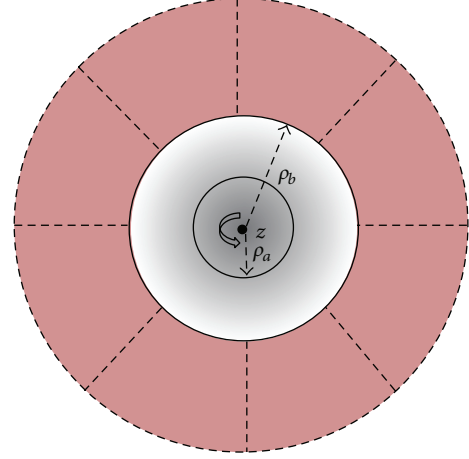


FIGURE 1: Cross-sectional view of a three-layer LCOF with the outermost section filled with liquid crystal (the dashed lines in the radial direction indicate the orientation of the liquid crystal molecules).

in the direction of propagation too. Of the liquid crystal section, the principal axes coincide with the  $z$ -axis, and the extraordinary principal axis is radially oriented. Therefore, the liquid crystal region will have the RI distribution as

$$n_\rho = n_e, \quad n_\phi = n_z \quad \text{with } n_e > n_1 > n_2 > n_o, \quad (1)$$

where  $n_\rho$ ,  $n_\phi$ , and  $n_z$  are, respectively, the RI values along the  $\rho$ -,  $\phi$ -, and  $z$ -directions. Now, following the formulations presented in [21], the coupled wave equations for the transverse field components can be written as [22]

$$\begin{aligned} & \left( \nabla_t^2 + k_0^2 n_\rho^2 - \beta^2 - \frac{1}{\rho^2} \right) e_\rho \\ &= -\frac{2}{\rho^2} \frac{\partial e_\phi}{\partial \phi} + \left( 1 - \frac{n_\rho^2}{n_z^2} \right) \frac{\partial}{\partial \rho} \left\{ \frac{1}{\rho} \frac{\partial}{\partial \rho} (\rho e_\rho) \right\} \\ &+ \left( 1 - \frac{n_\phi^2}{n_z^2} \right) \frac{\partial}{\partial \rho} \left( \frac{1}{\rho} \frac{\partial e_\phi}{\partial \phi} \right) \end{aligned} \quad (2a)$$

$$\begin{aligned} & \left( \nabla_t^2 + k_0^2 n_\phi^2 - \beta^2 - \frac{1}{\rho^2} \right) e_\phi \\ &= \frac{2}{\rho^2} \frac{\partial e_\rho}{\partial \phi} + \frac{1}{\rho^2} \left\{ \left( 1 - \frac{n_\rho^2}{n_z^2} \right) \frac{\partial}{\partial \rho} \left( \rho \frac{\partial e_\rho}{\partial \phi} \right) \right. \\ &\quad \left. + \left( 1 - \frac{n_\phi^2}{n_z^2} \right) \frac{\partial^2 e_\phi}{\partial \phi^2} \right\}, \end{aligned} \quad (2b)$$

where  $\nabla_t^2$  is the Laplacian operator in the cylindrical coordinate system and  $k_0$  is the free-space propagation constant.

Liquid crystal is anisotropic in nature, and therefore, the sustained modes in the LCOF under consideration will essentially contain the electric field components  $E_\rho$ ,  $E_\phi$ , and  $E_z$ , each facing different RI values in their respective

directions. However, in the present work, we consider the lower-order TE modes (namely, TE<sub>01</sub>). In this case, there is only one transverse electrical field component  $e_\phi$ , which is independent of the coordinate  $\phi$ , making thereby one to have  $e_\rho = 0$  and  $\partial e_\phi / \partial \phi = 0$  corresponding to this mode. Implementing these conditions and using (2a) and (2b), after some mathematical steps, it can be shown that the electric/magnetic field components in this case will be ultimately given as

$$H_\rho)_{\text{I}} = -C_1 \frac{\beta}{\omega \mu_0} J_1(\gamma_1 \rho) \exp\{j(\omega t - \beta z)\} \quad (3a)$$

$$H_z)_{\text{I}} = C_1 \frac{j}{\omega \mu_0} \left\{ \gamma_1 J_1'(\gamma_1 \rho) + \frac{1}{\rho} J_1(\gamma_1 \rho) \right\} \exp\{j(\omega t - \beta z)\} \quad (3b)$$

$$H_\rho)_{\text{II}} = -\frac{\beta}{\omega \mu_0} \{C_2 K_1(\gamma_2 \rho) + C_3 I_1(\gamma_2 \rho)\} \exp\{j(\omega t - \beta z)\} \quad (3c)$$

$$H_z)_{\text{II}} = \frac{j}{\omega \mu_0} \left[ C_2 \left\{ \gamma_2 K_1'(\gamma_2 \rho) + \frac{1}{\rho} K_1(\gamma_2 \rho) \right\} + C_3 \left\{ \omega I_1'(\gamma_2 \rho) + \frac{1}{\rho} I_1(\gamma_2 \rho) \right\} \right] \exp\{j(\omega t - \beta z)\} \quad (3d)$$

$$H_\rho)_{\text{III}} = -C_4 \frac{\beta}{\omega \mu_0} K_1(\gamma_3 \rho) \exp\{j(\omega t - \beta z)\} \quad (3e)$$

$$H_z)_{\text{III}} = C_4 \frac{j}{\omega \mu_0} \left\{ \gamma_3 K_1'(\gamma_3 \rho) + \frac{1}{\rho} K_1(\gamma_3 \rho) \right\} \times \exp\{j(\omega t - \beta z)\}. \quad (3f)$$

In (3a), (3b), (3c), (3d), (3e), and (3f), the superscripts I, II, and III, respectively, represent the situations in the LCOF core, inner clad and the outer liquid crystal clad sections of the guide. Also,  $\mu_0$  is the free-space permeability,  $C_1$ ,  $C_2$ ,  $C_3$ , and  $C_4$  are the arbitrary constants to be determined by the boundary conditions, and  $J(\cdot)$ ,  $K(\cdot)$ , and  $I(\cdot)$  represent Bessel and the modified Bessel functions. Further, the prime indicates the differentiation with respect to the argument, and the quantities  $\gamma_1$ ,  $\gamma_2$ , and  $\gamma_3$  are defined as

$$\gamma_1 = \sqrt{n_1^2 k_0^2 - \beta^2} \quad (4a)$$

$$\gamma_2 = \sqrt{\beta^2 - n_2^2 k_0^2} \quad (4b)$$

$$\gamma_3 = \sqrt{\beta^2 - n_0^2 k_0^2} \quad (4c)$$

Making use of the above-mentioned field components, as stated in (3a), (3b), (3c), (3d), (3e), and (3f) and implementing the electromagnetic boundary conditions at the layer interfaces of the LCOF, values of the arbitrary constants can be determined. By using those, the expressions corresponding

to power [23] transmitted through the different sections of the LCOF can be evaluated as

$$P_{\text{core}} = C_1^2 \frac{\pi}{\omega \mu_0} \left\{ \gamma_1 \int_0^{\rho_1} \rho J_1(\gamma_1 \rho) J_1'(\gamma_1 \rho) d\rho + \int_0^{\rho_2} \{J_1(\gamma_1 \rho)\}^2 d\rho \right\} \quad (5)$$

$$P_{\text{innerclad}} = C_1^2 \frac{\pi}{\omega \mu_0} \left[ \Psi^2 \left\{ \gamma_2 \int_{\rho_1}^{\rho_2} \rho I_1(\gamma_2 \rho) I_1'(\gamma_2 \rho) d\rho + \int_{\rho_1}^{\rho_2} (I_1(\gamma_2 \rho))^2 d\rho \right\} + \Omega^2 \left\{ \gamma_2 \int_{\rho_1}^{\rho_2} \rho K_1(\gamma_2 \rho) K_1'(\gamma_2 \rho) d\rho + \int_{\rho_1}^{\rho_2} (K_1(\gamma_2 \rho))^2 d\rho \right\} + \Phi \Psi \left\{ 2 \int_{\rho_1}^{\rho_2} K_1(\gamma_2 \rho) I_1(\gamma_2 \rho) d\rho + \gamma_2 \int_{\rho_1}^{\rho_2} \rho K_1(\gamma_2 \rho) I_1'(\gamma_2 \rho) d\rho + \gamma_2 \int_{\rho_1}^{\rho_2} \rho I_1(\gamma_2 \rho) K_1'(\gamma_2 \rho) d\rho \right\} \right] \quad (6)$$

$$P_{\text{outerclad}} = C_1^2 \frac{\pi}{\omega \mu_0} \left( \frac{\Phi K_1(\gamma_2 \rho_2) + \Psi I_1(\gamma_2 \rho_2)}{K_1(\gamma_3 \rho_2)} \right)^2 \times \left[ \int_{\rho_2}^{\infty} \{K_1(\gamma_3 \rho)\}^2 d\rho + \gamma_3 \int_{\rho_2}^{\infty} \rho K_1(\gamma_3 \rho) K_1'(\gamma_3 \rho) d\rho \right], \quad (7)$$

where

$$\Phi = \left( J_1(\gamma_1 \rho_1) \left\{ \gamma_2 I_1'(\gamma_2 \rho_1) + \frac{1}{\rho_1} K_1(\gamma_2 \rho_1) \right\} - I_1(\gamma_2 \rho_1) \left\{ \gamma_1 J_1'(\gamma_1 \rho_1) + \frac{1}{\rho_1} J_1(\gamma_1 \rho_1) \right\} \right) \times \left( K_1(\gamma_2 \rho_1) \left\{ \gamma_2 I_1'(\gamma_2 \rho_1) + \frac{1}{\rho_1} K_1(\gamma_2 \rho_1) \right\} - I_1(\gamma_2 \rho_1) \left\{ \gamma_2 K_1'(\gamma_2 \rho_1) + \frac{1}{\rho_1} K_1(\gamma_2 \rho_1) \right\} \right)^{-1}, \quad (8)$$

$$\Psi = \left( J_1(\gamma_1 \rho_1) \left\{ \gamma_2 K_1'(\gamma_2 \rho_1) + \frac{1}{\rho_1} K_1(\gamma_2 \rho_1) \right\} - K_1(\gamma_2 \rho_1) \left\{ \gamma_1 J_1'(\gamma_1 \rho_1) + \frac{1}{\rho_1} J_1(\gamma_1 \rho_1) \right\} \right)$$

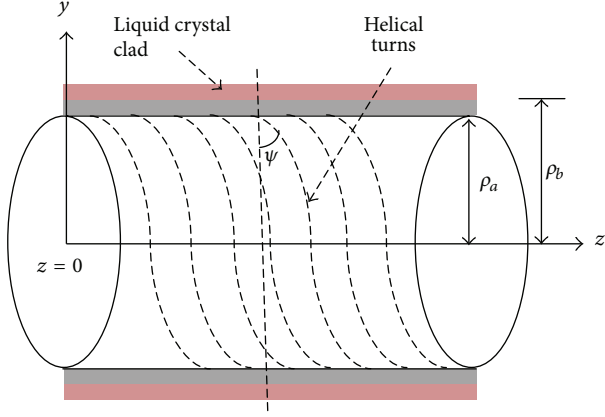


FIGURE 2: Longitudinal view of the HCLCOF under consideration.

$$\begin{aligned} & \times \left( I_1(\gamma_2 \rho_1) \left\{ \gamma_2 K_1'(\gamma_2 \rho_1) + \frac{1}{\rho_1} K_1(\gamma_2 \rho_1) \right\} \right. \\ & \left. - K_1(\gamma_2 \rho_1) \left\{ \gamma_2 I_1'(\gamma_2 \rho_1) + \frac{1}{\rho_1} K_1(\gamma_2 \rho_1) \right\} \right)^{-1}. \end{aligned} \quad (9)$$

Above derived (5), (6), and (7), respectively, represent the expressions of the power propagating through the LCOF core, inner dielectric clad, and the outer liquid crystal clad regions. It is to be noted at this point that the evaluation of power requires the values of all the arbitrary constants  $C_1$ ,  $C_2$ ,  $C_3$ , and  $C_4$  to be written in terms of only one constant (say  $C_1$ ), which can be determined by a normalization condition taking into consideration the input power. If  $P_{\text{total}}$  represents the total power transmitted through the LCOF by the  $TE_{01}$  modes, that is,

$$P_{\text{total}} = P_{\text{core}} + P_{\text{innerclad}} + P_{\text{outerclad}}, \quad (10)$$

then  $P_{\text{core}}/P_{\text{total}}$  ( $\equiv \Gamma_{\text{core}}$ ),  $P_{\text{innerclad}}/P_{\text{total}}$  ( $\equiv \Gamma_{\text{innerclad}}$ ), and  $P_{\text{outerclad}}/P_{\text{total}}$  ( $\equiv \Gamma_{\text{outerclad}}$ ) will, respectively, determine the relative power (or the power confinement factor) in the LCOF core, inner clad, and the outer clad sections.

**2.2. The Case of HCLCOFs.** Figure 2 shows the longitudinal view of the HCLCOF under consideration, which incorporates some modifications in the previous guide structure illustrated in Figure 1 in the form of additional conducting helical windings loaded at the interface of the core and the inner dielectric clad sections. As the fiber core is wrapped with a conducting sheath helix at a constant angle (called as the helix pitch angle)  $\psi$  around the core-inner clad boundary, the structure essentially has a circular cylindrical surface with high conductivity in a preferential direction. This way, helical clad fibers offer the additional parameter to suitably control the modal behaviour of the guide, that is, by varying the pitch angle of helix—an aspect of great technological importance [17–20].

Coming to the analytical steps, the field components in the different sections of the HCLCOFs will be represented by

(3a), (3b), (3c), (3d), (3e), and (3f). However, the boundary conditions will be modified in this case [24], the implementation of which will finally provide an  $8 \times 8$  determinant formed by the coefficients of the unknown constants. A nontrivial solution to the set of equations can be obtained if the determinant is equated to zero, that is,

$$\begin{pmatrix} x_1 & x_2 & 0 & 0 & 0 & 0 & 0 & 0 \\ 0 & 0 & x_3 & x_4 & x_5 & x_6 & 0 & 0 \\ x_7 & -x_8 & -x_9 & -x_{10} & x_{11} & x_{12} & 0 & 0 \\ -x_{13} & x_{14} & x_{15} & x_{16} & -x_{17} & -x_{18} & 0 & 0 \\ 0 & 0 & y_1 & y_2 & y_3 & y_4 & 0 & 0 \\ 0 & 0 & 0 & 0 & 0 & 0 & y_5 & y_6 \\ 0 & 0 & y_7 & y_8 & -y_9 & -y_{10} & -y_{11} & y_{12} \\ 0 & 0 & -y_{13} & -y_{14} & y_{15} & y_{16} & y_{17} & -y_{18} \end{pmatrix} \times \begin{pmatrix} A \\ B \\ C \\ D \\ E \\ F \\ G \\ H \end{pmatrix} = \begin{pmatrix} 0 \\ 0 \\ 0 \\ 0 \\ 0 \\ 0 \\ 0 \\ 0 \end{pmatrix}. \quad (11)$$

In (11), the used symbols have their meanings as

$$x_1 = \left( \sin \psi + \frac{\nu \beta}{\gamma_1^2 \rho_a} \cos \psi \right) J_\nu(\gamma_1 \rho_a),$$

$$x_2 = \frac{i\omega\mu_0}{\gamma_1} \cos \psi J_\nu'(\gamma_1 \rho_a),$$

$$x_3 = \left( \sin \psi + \frac{\nu \beta}{\gamma_2^2 \rho_a} \cos \psi \right) K_\nu(\gamma_2 \rho_a),$$

$$x_4 = \left( \sin \psi + \frac{\nu \beta}{\gamma_2^2 \rho_a} \cos \psi \right) I_\nu(\gamma_2 \rho_a),$$

$$x_5 = \frac{i\omega\mu_0}{\gamma_2} \cos \psi K_\nu'(\gamma_2 \rho_a),$$

$$x_6 = \frac{i\omega\mu_0}{\gamma_2} \cos \psi I_\nu'(\gamma_2 \rho_a),$$

$$x_7 = \left( \cos \psi - \frac{\nu \beta}{\gamma_1^2 \rho_a} \sin \psi \right) J_\nu(\gamma_1 \rho_a),$$

$$x_8 = \frac{i\omega\mu_0}{\gamma_1} J_\nu'(\gamma_1 \rho_a),$$

$$x_9 = \left( \cos \psi - \frac{\nu \beta}{\gamma_2^2 \rho_a} \sin \psi \right) K_\nu(\gamma_2 \rho_a),$$

$$x_{10} = \left( \cos \psi - \frac{\nu \beta}{\gamma_2^2 \rho_a} \sin \psi \right) I_\nu(\gamma_2 \rho_a),$$

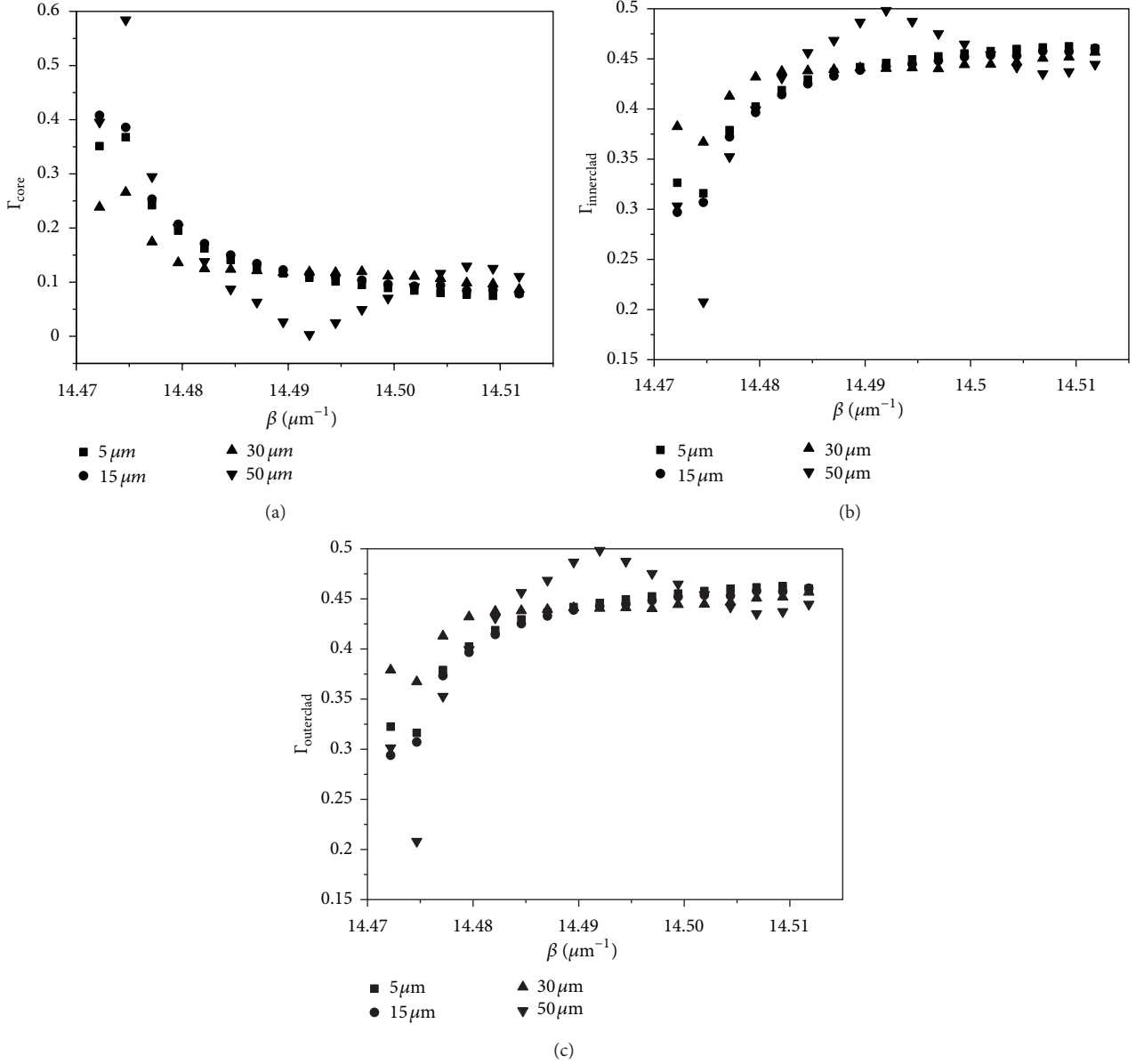


FIGURE 3: (a) Power confinement by the TE modes in the LCOF core. (b) Power confinement by the TE modes in the LCOF inner clad. (c) Power confinement by the TE modes in the LCOF outer clad.

$$\begin{aligned}
 x_{11} &= \frac{i\omega\mu_0}{\gamma_2} \sin \psi K'_v(\gamma_2\rho_a), & x_{17} &= \left( \sin \psi + \frac{\nu\beta}{\gamma_2^2\rho_a} \cos \psi \right) K_v(\gamma_2\rho_a), \\
 x_{12} &= \frac{i\omega\mu_0}{\gamma_2} \sin \psi I'_v(\gamma_2\rho_a), & x_{18} &= \left( \sin \psi + \frac{\nu\beta}{\gamma_2^2\rho_a} \cos \psi \right) I_v(\gamma_2\rho_a), \\
 x_{13} &= \frac{i\omega\varepsilon_1}{\gamma_1} \cos \psi J'_v(\gamma_1\rho_a), & y_1 &= \left( \sin \psi + \frac{\nu\beta}{\gamma_2^2\rho_b} \cos \psi \right) K_v(\gamma_2\rho_b), \\
 x_{14} &= \left( \sin \psi + \frac{\nu\beta}{\gamma_1^2\rho_a} \cos \psi \right) J_v(\gamma_1\rho_a), & y_2 &= \left( \sin \psi + \frac{\nu\beta}{\gamma_2^2\rho_b} \cos \psi \right) I_v(\gamma_2\rho_b), \\
 x_{15} &= \frac{i\omega\varepsilon_2}{\gamma_2} \cos \psi K'_v(\gamma_2\rho_a), & y_3 &= \frac{i\omega\mu_0}{\gamma_2} \cos \psi K'_v(\gamma_2\rho_b), \\
 x_{16} &= \frac{i\omega\varepsilon_2}{\gamma_2} \cos \psi I'_v(\gamma_2\rho_a), & y_4 &= \frac{i\omega\mu_0}{\gamma_2} \cos \psi I'_v(\gamma_2\rho_b),
 \end{aligned}$$

$$\begin{aligned}
y_5 &= \left( \sin \psi + \frac{\nu\beta}{\gamma_3^2 \rho_b} \cos \psi \right) K_\nu(\gamma_3 \rho_b), \\
y_6 &= \frac{i\omega\mu_0}{\gamma_3} \cos \psi K'_\nu(\gamma_3 \rho_b), \\
y_7 &= \left( \cos \psi - \frac{\nu\beta}{\gamma_2^2 \rho_b} \sin \psi \right) K_\nu(\gamma_2 \rho_b), \\
y_8 &= \left( \cos \psi - \frac{\nu\beta}{\gamma_2^2 \rho_b} \sin \psi \right) I_\nu(\gamma_2 \rho_b), \\
y_9 &= \frac{i\omega\mu_0}{\gamma_2} K'_\nu(\gamma_2 \rho_b), \\
y_{10} &= \frac{i\omega\mu_0}{\gamma_2} I'_\nu(\gamma_2 \rho_b), \\
y_{11} &= \left( \cos \psi - \frac{\nu\beta}{\gamma_3^2 \rho_b} \sin \psi \right) K_\nu(\gamma_3 \rho_b), \\
y_{12} &= \frac{i\omega\mu_0}{\gamma_3} \sin \psi K'_\nu(\gamma_3 \rho_b), \\
y_{13} &= \frac{i\omega\varepsilon_2}{\gamma_2} \cos \psi K'_\nu(\gamma_2 \rho_b), \\
y_{14} &= \frac{i\omega\varepsilon_2}{\gamma_2} \cos \psi K'_\nu(\gamma_2 \rho_b), \\
y_{15} &= \left( \sin \psi + \frac{\nu\beta}{\gamma_2^2 \rho_b} \cos \psi \right) K_\nu(\gamma_2 \rho_b), \\
y_{16} &= \left( \sin \psi + \frac{\nu\beta}{\gamma_2^2 \rho_b} \cos \psi \right) I_\nu(\gamma_2 \rho_b), \\
y_{17} &= \frac{i\omega\varepsilon_3}{\gamma_3} \cos \psi K'_\nu(\gamma_3 \rho_b), \\
y_{18} &= \left( \sin \psi + \frac{\nu\beta}{\gamma_3^2 \rho_b} \cos \psi \right) K_\nu(\gamma_3 \rho_b).
\end{aligned} \tag{12}$$

Equation (11) is the eigenvalue equation corresponding to the HCLCOF structure, solutions to which will provide the modes sustained in the guide.

### 3. Results and Discussion

The two types of fiber structures, namely, the LCOF and the HCLCOF, can now be analyzed. In the case of LCOF, the relative distributions of power in the three different regions of the guide are considered, whereas the analyses corresponding to HCLCOF are limited to the modal dispersion relations and the field cutoffs. Figures 3(a), 3(b), and 3(c), respectively, illustrate the nature of power propagation in the LCOF core, inner clad, and the outer clad regions, as plotted against the propagation constant  $\beta$  corresponding to the situation of TE mode excitation in the guide. In our illustrative cases, we consider four different values of core radius for

the computational purpose, namely,  $5 \mu\text{m}$ ,  $15 \mu\text{m}$ ,  $30 \mu\text{m}$ , and  $50 \mu\text{m}$ , and the clad radius is kept fixed at  $125 \mu\text{m}$ . Further, the RI values of core and the inner clad regions are taken to be  $n_1 = 1.462$  and  $n_2 = 1.458$ , respectively, and the operating wavelength  $\lambda_0$  is kept fixed as  $633 \text{ nm}$ . The outermost region of the guides (LCOF and HCLCOF) is considered to be the nematic liquid crystal named as BDH mixture 14616, which has the ordinary and the extraordinary RI values as  $n_o = 1.457$  and  $n_e = 1.5037$ , respectively.

Now, focussing on the computations of the relative distribution of power in LCOF, we observe from Figure 3(a) that the confinement of power shows an initial increase with the propagation constant  $\beta$  corresponding to almost all the fiber core dimensions considered here. However, the increase is more prominent in the case of LCOFs of larger core radius. We further find that, near the higher  $\beta$ -tail, power confinements are observed to be increasing with that of the core dimensions, which is very much expected as the fibers of larger dimensions essentially possess the capability of confining more amount of power in the fiber core. In the lower  $\beta$ -tail regime, we observe some fluctuations in power, and corresponding to  $50 \mu\text{m}$  core radius, almost 59% of power is confined into the core section. In the medium range of the allowed propagation constants, the confinement patterns exhibit a kind of uniformity corresponding to lower dimensions of the LCOF. The largest core radius chosen here is  $50 \mu\text{m}$ , and the confinement shows more fluctuations corresponding to this case. This is attributed to the fact that the LCOF becomes extremely multimode in this case, resulting thereby some sort of modal interference, which affects the uniformity in the distribution of power. The feature related to the kind of uniform power distribution over propagating modes is more required in telecommunication purposes, and LCOFs of smaller dimensions would possibly meet the requirements. However, more promising needs of LCOFs are expected to be in optical sensing or other integrated optic applications, which would generally require more amount of power to be confined in the outermost clad. Figure 3(a) shows the confinement to be almost about 15%–25% distributed over major portion of the allowed values of propagation constants.

Figures 3(b) and 3(c), respectively, correspond to the relative distribution of power in the LCOF inner dielectric and the outer liquid crystal clad sections. We observe that the power confinement patterns are almost similar in both of these sections, and also, the trends of power patterns are just opposite to what we observed in the LCOF core, which is quite expected as the way confinement increases or decreases (with the propagation constant) in the core section, it will decrease or increase, respectively, in the two clads. The noticeable fact remains that the average value of power in the two clad sections is appreciably higher (within the longer  $\beta$ -range) than what is observed in the LCOF core. More precisely, corresponding to lower LCOF core dimensions, within the uniform range of the allowed values of propagation constants, approximately 45% power is shared by each of the clad regions, whereas around only 10% power transmission is observed in the LCOF core at the same time. This essentially indicates a substantial increase of power in

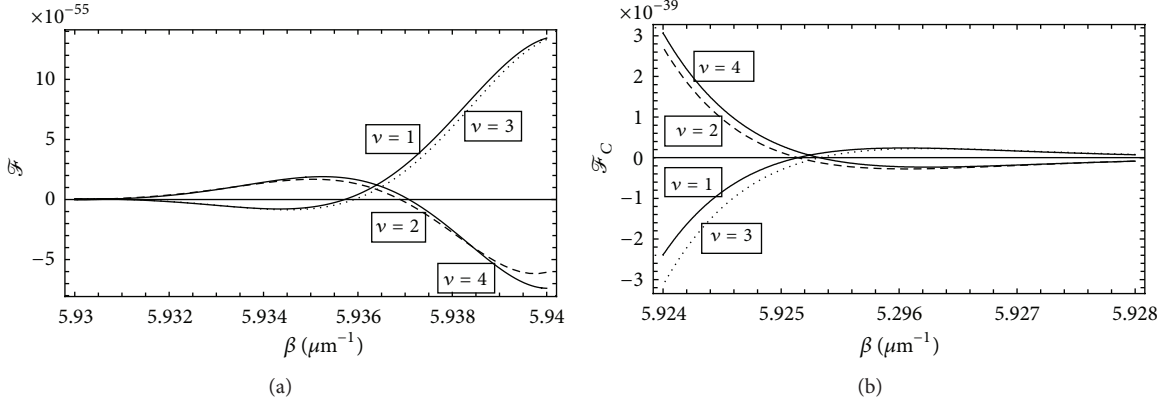


FIGURE 4: (a) Plot of the dispersion relation for the TE modes corresponding to  $\psi = 0^\circ$ . (b) Plot of the cutoff characteristics for the TE modes corresponding to  $\psi = 0^\circ$ .

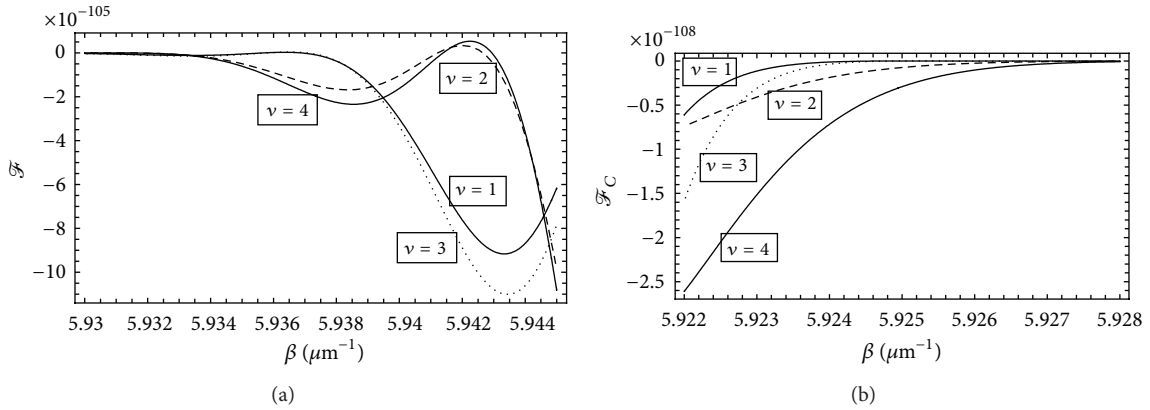


FIGURE 5: (a) Plot of the dispersion relation for the TE modes corresponding to  $\psi = 90^\circ$ . (b) Plot of the cutoff characteristics for the TE modes corresponding to  $\psi = 90^\circ$ .

the two clad sections, which is attributed to the presence of nematic radially anisotropic liquid crystal material in the outermost clad region. The distribution of power, however, does not seem to be that uniform in the lower  $\beta$ -tail regime, and the uniformity is more affected with the increase in core dimension owing to the reason of possibilities related to modal interference in this case. Finally, the combined observations of the uniformity of power patterns corresponding to the LCOFs of smaller dimensions and higher power confinements in the outermost liquid crystal section (Figures 3(a) and 3(b)) essentially indicate the possibility of useful integrated optic applications of these guides, for example, in field coupling and/or optical sensing needs.

Now, turning the attention towards the case of HCLCOFs, we make an attempt to study the dispersion relation expressed by (11). In this stream, we consider the values of the fiber core radius as  $60.38 \mu\text{m}$  and the inner clad radius as  $120.07 \mu\text{m}$ . The operating wavelength is chosen as  $1.55 \mu\text{m}$ , and the RI values of the core and the inner clad sections are taken to be 1.5 and 1.46, respectively. The physical properties of the outermost liquid crystal section are considered to be the same as in the case of LCOF discussed above. Equation (11) is plotted corresponding to four different values of the

azimuthal index  $\nu$ , namely,  $\nu = 1$ ,  $\nu = 2$ ,  $\nu = 3$ , and  $\nu = 4$ , and the introduced conducting helical turns may have perpendicular or parallel orientations with respect to the optical axis, making thereby the respective helical pitch angles as  $\psi = 0^\circ$  and  $\psi = 90^\circ$ .

Figure 4(a) illustrates the plots of the left hand side  $\mathcal{F}$  of (6) in the case when the helix pitch angles are perpendicular to the optical axis, that is,  $\psi = 0^\circ$ . In this case, we observe that, corresponding to all values of the azimuthal indices, the plots intersect the  $\mathcal{F} = 0$  axis; the points of intersection essentially determine the propagation constant of the corresponding mode. We observe that the modal propagation constants corresponding to  $\nu = 1$  and  $\nu = 3$  are very close, though with the situation  $\beta_{\nu=1} \leq \beta_{\nu=2}$ . Further, the modes with  $\nu = 2$  and  $\nu = 4$  attain almost similar  $\beta$ -values with  $\beta_{\nu=2} \leq \beta_{\nu=4}$ .

Figure 4(b) describes the situation when (11) is solved under the limit  $\gamma_2^2 \rightarrow 0$ , indicating thereby the respective plots (of  $\mathcal{F}_C$ ) to correspond the case of field cutoffs. We observe that the cutoffs for the modes with  $\nu = 1$  and  $\nu = 3$  are almost the same, and that with  $\nu = 2$  and  $\nu = 4$  too are very much similar. However, we observe from Figures 4(a) and 4(b) that the cutoff  $\beta$ -values, as seen in Figure 4(b), are less than that obtained from the knowledge of

$\beta$ -values noticed from the intersections in Figure 4(a), which essentially concludes that the results illustrated in Figures 4(a) and 4(b) are consistent.

It is noteworthy that the helix pitch angle  $\psi$  introduced in HCLCOF has the ability to alter the dispersion characteristics of the guide. In order to demonstrate this, plots are made corresponding to  $90^\circ$  pitch, and those corresponding to the dispersion equation and the field cutoffs are illustrated in Figures 5(a) and 5(b). In both these figures, profound effect due to helix pitch can clearly be observed. It is found that the  $\beta$ -values are roughly increased in this case. Making the pitch  $\psi = 90^\circ$  leaves the impression of eliminating the helical turns as those are now oriented just parallel to the optical axis. Thus, it can be conceptually understood that the presence of conducting helical turns (i.e.,  $\psi = 0^\circ$ ) introduces the modal propagation constants to be lower. It has been reported before that helix pitch makes the propagating waves to attenuate up to some extent—the property which can clearly be seen in the case of HCLCOF as the waves propagate with lower propagation constants under the perpendicular orientation (with respect to the optical axis) of helical turns.

#### 4. Conclusion

From the foregoing discussions, inference can be drawn that, under TE mode excitation, LCOFs present higher amount of power confinement in the inner dielectric and the outer liquid crystal clads—the feature that can be effectively used in several integrated optic applications including electromagnetic field coupling and optical sensing. It has been found that, with the increase in propagation constants, the confinement patterns become almost uniform, which is not observed corresponding to LCOFs of higher core diameters. Higher confinement of power in the cladding regions can be interpreted as if the power is leaking off the LCOF core, and this feature can be attributed to the presence of radially anisotropic liquid crystal material in the outermost section of the guide.

Furthermore, the fundamental investigations of HCLCOFs reveal that the introduction of conducting helical windings at the interface of the core-inner dielectric clad sections makes the guide to attain the attenuation property. The possibility of suitable adjustments of the helix pitch leaves the option to alter the attenuation characteristics of the guide, the feature quite indispensable in several optical applications.

#### Acknowledgment

The author gratefully acknowledges the financial support given by the Ministry of Higher Education (Malaysia) through the Fundamental Research Grant project no. (FRGS/1/2011/TK/UKM/01/16).

#### References

- [1] A. Jákli, D. Krüerke, and G. G. Nair, “Liquid crystal fibers of bent-core molecules,” *Physical Review E*, vol. 67, no. 5, Article ID 051702, 6 pages, 2003.
- [2] T. R. Wolinski, K. Szaniawska, S. Ertman et al., “Influence of temperature and electrical fields on propagation properties of photonic liquid-crystal fibres,” *Measurement Science and Technology*, vol. 17, no. 5, pp. 985–991, 2006.
- [3] T. R. Wolinski, S. Ertman, A. Czaplá et al., “Polarization effects in photonic liquid crystal fibres,” *Measurement Science and Technology*, vol. 18, pp. 3061–3069, 2007.
- [4] B. P. Cumming, A. Jesacher, M. J. Booth, T. Wilson, and M. Gu, “Adaptive aberration compensation for three-dimensional micro-fabrication of photonic crystals in lithium niobate,” *Optics Express*, vol. 19, pp. 9419–9425, 2011.
- [5] Y. Fu, F. Barnes, T. Ewing, S. Serati, and X. W. Xia, “Liquid crystal modulated optical CDMA in a fiber-based testbed,” in *Active and Passive Optical Components for WDM Communications IV*, vol. 5595 of *Proceedings of SPIE*, pp. 302–309, October 2004.
- [6] S. T. Wu and U. Efron, “Optical properties of thin nematic liquid crystal cells,” *Applied Physics Letters*, vol. 48, pp. 624–636, 1986.
- [7] I. Sage and D. Chaplin, “Low RI liquid crystals for integrated optics,” *Electronics Letters*, vol. 23, no. 22, pp. 1192–1193, 1987.
- [8] M. Green and S. J. Madden, “Low loss nematic liquid crystal cored fiber waveguides,” *Applied Optics*, vol. 28, pp. 5202–5203, 1989.
- [9] H. Lin, P. P. Muhoray, and M. A. Lee, “Liquid crystalline cores for optical fibers,” *Molecular Crystals and Liquid Crystals*, vol. 204, pp. 189–200, 1991.
- [10] C. Veilleux, J. Lapiere, and J. Bures, “Liquid-crystal-clad tapered fibers,” *Optics Letters*, vol. 11, pp. 733–735, 1986.
- [11] S. H. Chen and T. J. Chen, “Observation of mode selection in a radially anisotropic cylindrical waveguide with liquid-crystal cladding,” *Applied Physics Letters*, vol. 64, no. 15, pp. 1893–1895, 1994.
- [12] Z. K. Ioannidis, I. P. Giles, and C. Bowry, “All-fiber optic intensity modulators using liquid crystals,” *Applied Optics*, vol. 30, pp. 328–333, 1991.
- [13] E. S. Goldburt and P. S. J. Russell, “Electro-optical response of a liquid-crystalline fiber coupler,” *Applied Physics Letters*, vol. 48, no. 1, pp. 10–12, 1986.
- [14] T. Yoshino, Y. Takahashi, H. Tamura, and N. Ohde, “Some special fibers for distributed sensing of uv light, electric field or strain,” in *Distributed and Multiplexed Fiber Optic Sensors III*, vol. 2071 of *Proceedings of SPIE*, pp. 242–254, December 1993.
- [15] P. K. Choudhury and W. K. Soon, “On the transmission by liquid crystal tapered optical fibers,” *Optik*, vol. 122, no. 12, pp. 1061–1068, 2011.
- [16] J. R. Pierce, *Travelling Wave Tubes*, D. Van Nostrand, Princeton, NJ, USA, 1950.
- [17] C. C. Siong and P. K. Choudhury, “Propagation characteristics of tapered core helical clad dielectric optical fibers,” *Journal of Electromagnetic Waves and Applications*, vol. 23, no. 5, pp. 663–674, 2009.
- [18] A. H. B. M. Safie and P. K. Choudhury, “On the hybrid field patterns of helical clad dielectric optical fibers,” *Progress in Electromagnetics Research*, vol. 91, pp. 69–84, 2009.
- [19] K. Y. Lim, P. K. Choudhury, and Z. Yusoff, “Chirifibers with helical windings—an analytical investigation,” *Optik*, vol. 121, no. 11, pp. 980–987, 2010.
- [20] P. K. Choudhury and D. Kumar, “On the slow-wave helical clad elliptical fibers,” *Journal of Electromagnetic Waves and Applications*, vol. 24, no. 14–15, pp. 1931–1942, 2010.
- [21] A. W. Snyder and F. Rühl, “Single-mode, single-polarization fibers made of birefringent material,” *Journal of the Optical Society of America*, vol. 73, pp. 1165–1174, 1983.

- [22] Y. Chen, "Anisotropic fiber with cylindrical polar axes," *Applied Physics B*, vol. 42, no. 1, pp. 1-3, 1987.
- [23] A. H. Cherin, *An Introduction to Optical Fibers*, chapter 5, McGraw-Hill, New York, NY, USA, 1987.
- [24] D. A. Watkins, *Topics in Electromagnetic Theory*, Wiley, New York, NY, USA, 1958.

## Research Article

# Temperature Dependence of the Tilt Angle for the Smectic A-Smectic C\* Transition in a Mixture of C7-70PDOB Ferroelectric Liquid Crystals near the Tricritical Point

Mustafa Kurt<sup>1</sup> and Hamit Yurtseven<sup>2</sup>

<sup>1</sup>Department of Physics, Canakkale Onsekiz Mart University, 17100 Canakkale, Turkey

<sup>2</sup>Department of Physics, Middle East Technical University, 06531 Ankara, Turkey

Correspondence should be addressed to Hamit Yurtseven, hamit@metu.edu.tr

Received 12 June 2012; Accepted 12 September 2012

Academic Editor: Durga Ojha

Copyright © 2012 M. Kurt and H. Yurtseven. This is an open access article distributed under the Creative Commons Attribution License, which permits unrestricted use, distribution, and reproduction in any medium, provided the original work is properly cited.

The temperature dependence of the tilt angle  $\theta$  is studied in the smectic C\* phase near the smectic A-smectic C\* tricritical point for a mixture of 70PDOB in the ferroelectric liquid crystal C7 ( $X = 16.92$ ). The mean-field models with the biquadratic  $P^2\theta^2$  ( $P$  is the spontaneous polarization) and  $P^2\theta^2 + P\theta$  (bilinear) coupling terms in the free energy expansion are used to analyze the experimental data for the tilt angle in this binary mixture. From our analysis, the coefficients given in the free energy expansion of the mean-field models are determined. Our results show that the mean-field theory explains adequately the observed behaviour of the C7-70PDOB mixture near the AC\* tricritical point.

## 1. Introduction

Smectic transitions in ferroelectric liquid crystals have been the subject of various experimental and theoretical studies. In particular, smectic A and C (or C\*) transitions have been investigated and reported in the literature.

In the smectic A phase, the liquid molecules are oriented along the director (orientational order parameter) and they show a transitional order in layers, whereas in the smectic C (or C\*) phase, additionally they make a tilt angle with the director which is perpendicular to the smectic layers. If the chiral molecules, which are optically active, exist in the liquid crystalline material, then the smectic C\* phase occurs.

The smectic A-smectic C\* (AC\*) transition has been predicted by de Gennes [1] as the transition which belongs to the three-dimensional XY universality class ( $n = 2, n = 3$ ). This has not been confirmed by some early experiments which are in agreement with a Landau mean-field theory of the AC\* transition [2–7]. Some experimental [8–13] and theoretical [3, 14, 15] studies have shown that from the first-order to a second order AC\* transition, there occurs a tricritical point (TCP). In our recent studies, tricritical

behaviour of mixtures of C7+10.04 [16] and SCE9+SCE10 [17, 18] has been shown using the mean-field models. Mean-field models are applicable to many liquid crystalline systems and they predicted adequately the observed behaviour of those materials exhibiting phase transitions. The physical quantities measured to high accuracy can then be analyzed by a mean-field model and the type of transition (first order, second order, or tricritical) can be characterized. From this point of view, mean-field model is a more realistic theoretical model to be applicable to the experiments.

The mean-field models which describe the AC (or AC\*) transitions have the free energy expanded in terms of the order parameters (tilt angle  $\theta$  and the spontaneous polarization  $P$ ) and their bilinear ( $P\theta$ ) and/or biquadratic ( $P^2\theta^2$ ) couplings [3, 14, 19, 20]. Dipolar interactions ( $P\theta$  coupling) are of a chiral character which becomes importantly close to the AC\* transition, whereas quadrupolar interactions ( $P^2\theta^2$  coupling) are of a nonchiral one which covers a wide range of temperatures below the transition temperature in the smectic C or AC\* phase. On the basis of our earlier mean-field models with the biquadratic coupling ( $P^2\theta^2$ ), recently we have calculated tilt angle and the temperature shifts

as a function of concentration for a mixture of 10.04+C7 [16] and the temperature dependence of the spontaneous polarization and the tilt angle for a mixture of SCE9+SCE10 [17, 18] for the AC\* transition. Very recently, we have studied the dielectric constant as a function of temperature for the AC\* transition in 4-(3-methyl-2-chlorobutanoyloxy)-4'-heptyloxybiphenly (A7) [21] and we have calculated a generalized smectic-hexatic phase diagram in various mixtures of liquids crystals [22].

In this study, we focus on the temperature dependence of the tilt angle for a mixture of C7-70PDOB ferroelectric liquid crystal close to the tricritical point (TCP). The ferroelectric material 4-(3-methyl-2-chlorobutanoyloxy)-4'-heptyloxy biphenly (C7) exhibits a large spontaneous polarization [11]. It undergoes a first-order AC\* transition. When adding a second compound of 4-heptyloxy-4'-decloxybenzoate (7OPDOB), this transition is driven towards a second order by passing through a tricritical point (TCP) [9]. The transition temperatures of C7 for the relevant phases are as follows: SmC\* (53.9°C) and SmA (54.06°C) [8]. The AC\* transition temperatures of a binary mixture of C7+7OPDOB depending on the  $X$  values (mol percent of 7OPDOB) [9] are given in Table 1. Ferroelectric liquid crystals with large spontaneous polarizations such as C7 can be used in switching display devices and liquid crystals devices. Their carbon-13 nuclear magnetic resonance can be obtained experimentally to determine the temperature dependence of order parameter. In our previous study [21], we used our mean-field model with the  $P^2\theta^2$  coupling and calculated the dielectric constant (dielectric susceptibility) at various temperatures under constant electric field for A7. Our calculation for the tilt angle (order parameter) as a function of temperature was performed [21] using the molecular field theory [23] for A7. The experimental data for the dielectric constant of A7 [24] was then analyzed according to the expression derived from the mean-field model [21]. Similarly, we have used our mean-field model with the quadratic couplings  $\Psi^2\theta^2$  ( $\Psi$  is the orientational order parameter and  $\theta$  is the tilt angle) for the smectic-hexatic phase transitions in various mixtures of liquid crystals in our recent study [22]. By expanding the free energy in terms of the order parameters ( $\Psi$  and  $\theta$ ), we derived the phase line equations and calculated a generalized phase diagram ( $T$ - $X$ ) on the basis of the experimental data [25].

In the present study, not only the quadric coupling  $P^2\theta^2$  but also  $P^2\theta^2 + P\theta$  coupling in the free energy of our mean-field model is considered and the temperature dependence of the tilt angle  $\theta$  is derived in both cases. Instead of using the temperature dependence of the order parameter from the order parameter, from the molecular field theory [23], as we have also needed in our recent study [21], the  $\theta$  versus  $T$  relation derived here is directly used to analyze the experimental data [9]. This is more general in the sense that the experimental data can be analyzed freely with the fitted parameters determined, whereas the molecular field theory [23] predicts the temperature dependence of the order parameter according to the critical exponent 1/2. This, however, can restrict the analysis of the experimental data for

various mixtures of liquid crystals. In order to get good fits, our  $\theta$  versus  $T$  expression is favorable. On this basis, we have fitted to the experimental data [9] the expression for the tilt angle as a function of temperature, which we derive from the mean-field models with the  $P^2\theta^2$  and  $P\theta + P^2\theta^2$  couplings for the AC\* transition close to the TCP. Coefficients given in the mean-field energy are calculated from our fits and they are interpreted within the AC\* transition in this mixture of C7-70PDOB.

In Section 2, we give an outline of our mean-field models, where the temperature dependence of the tilt angle and the spontaneous polarization are derived. In Section 3, the tilt angle expression is fitted to the experimental data and the results are presented. Sections 4 and 5 give our discussion and conclusions, respectively.

## 2. Theory

The free energy of the smectic C\* phase can be expanded in terms of the tilt angle  $\theta$  and the spontaneous polarization  $P$  for the AC\* transition in ferroelectric liquid crystals. By considering the quadrupolar interaction between the  $\theta$  and  $P$  (biquadratic coupling  $P^2\theta^2$ ), the free energy can be expressed as

$$g = \frac{1}{2}a(T - T_0)\theta^2 + \frac{1}{4}b\theta^4 + \frac{1}{6}c\theta^6 + \frac{1}{2\chi_0\epsilon_0}P^2 - DP^2\theta^2 + \frac{1}{4}eP^4 - EP \quad (1)$$

in the presence of the electric field  $E$ , where  $a$ ,  $b$ ,  $c$ ,  $D$ , and  $e$  are constants.  $T_0$  is the transition temperature,  $\chi_0$  is the static dielectric susceptibility, and  $\epsilon_0$  is the permittivity in free space. In the free energy expansion, the tilt angle  $\theta$  is taken as the primary order parameter which does not exist in the smectic A phase. The spontaneous polarization  $P$  is the secondary order parameter which is defined in both the smectic A and C\* phases. We have introduced this model in our previous study [19].

In order to describe the AC\* transition, the energy is minimized with respect to the order parameters  $P$  and  $\theta$ . By minimizing the free energy  $g$  with respect to the spontaneous polarization  $P$ , we get at the zero electric field ( $E = 0$ ),

$$\frac{1}{\chi_0\epsilon_0} - 2D\theta^2 + eP^2 = 0. \quad (2)$$

Also, by minimizing the free energy  $g$  with respect to the tilt angle  $\theta$ , we find that

$$a(T - T_0) + b\theta^2 + c\theta^4 - 2DP^2 = 0. \quad (3)$$

Equations (2) and (3) give the temperature dependence of the spontaneous polarization and tilt angle, respectively. By substituting (2) into (3), the temperature dependence of the primary order parameter  $\theta$  (tilt angle) can be written as

$$(T - T_C) = \frac{-c}{a}\theta^4 + \frac{1}{a}\left(\frac{4D^2}{e} - b\right)\theta^2 - \frac{3}{16 \cdot c \cdot a}\left(b - \frac{4D^2}{e}\right)^2. \quad (4)$$

TABLE 1: Transition temperature ( $T_{AC^*}$ ) for the different mixtures of C7+7OPDOB system [9].

Mole percent	$T_{AC^*}$ (°C)
16.92	44.668
15.49	45.120
14.02	45.738
13.60	46.095
13.30	46.271

In (4) the temperature shifts,

$$\Delta T = T_C - T_0 = \frac{3}{16ac} \left( b - \frac{4D^2}{e} \right)^2 - \frac{2D}{e\alpha\chi_0\epsilon_0}, \quad (5)$$

were used for a first-order AC\* transition [19]. In (5)  $T_C$  denotes the experimentally measured AC\* transition.

The free energy of the smectic C\* phase can also be expanded in terms of the tilt angle  $\theta$  and the spontaneous polarization  $P$  by considering both the dipolar interactions (bilinear coupling  $P\theta$ ) and the quadrupolar interactions (biquadratic coupling  $P^2\theta^2$ ) for the AC\* transition in ferroelectric liquid crystals. The free energy can then be expressed as

$$g = \frac{1}{2}a(T - T_0)\theta^2 + \frac{1}{2}b\theta^4 + c\theta^6 + \frac{1}{2\chi_0\epsilon_0}P^2 - DP^2\theta^2 - CP\theta. \quad (6)$$

By minimizing the free energy with respect to the spontaneous polarization  $P$  and the tilt angle  $\theta$  as before, one gets

$$\frac{P}{\chi_0\epsilon_0} - C\theta - 2DP\theta^2 = 0, \quad (7)$$

$$a(T - T_0)\theta + b\theta^3 + c\theta^5 - CP - 2DP^2\theta = 0, \quad (8)$$

respectively. By substituting (7) into (8), the temperature dependence of the tilt angle  $\theta$  can be written as

$$(T - T_0) = \frac{-b}{a}\theta^2 - \frac{c}{a}\theta^4 + \frac{1}{a} \left( \frac{\chi_0\epsilon_0 C^2}{1 - 2D\chi_0\epsilon_0\theta^2} \right) + \frac{1}{a} \left( \frac{2D\chi_0^2\epsilon_0^2 C^2\theta^2}{(1 - 2D\chi_0\epsilon_0\theta^2)^2} \right). \quad (9)$$

Using (1) and (6) with the  $P^2\theta^2$  and  $P^2\theta^2 + P\theta$  coupling in the free energies, respectively, the temperature dependence of the tilt angle  $\theta$  can be predicted for the AC\* transition in ferroelectric liquid crystals.

### 3. Calculations and Results

The temperature dependence of the tilt angle  $\theta$  was calculated for the AC\* transition of a binary mixture of 70PDOB in C7 near the tricritical point ( $X = 16.92$ ). The value  $X$  is the mol percent (mol %) of 70PDOB in C7, as given in Table 1 [9]. For this calculation, (4) was

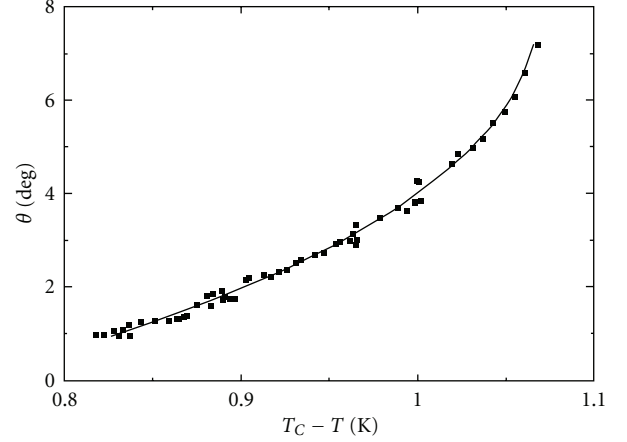


FIGURE 1: Tilt angle  $\theta$  as a function of  $T - T_C$  for the AC\* transition in a mixture of 70PDOB+C7 near the tricritical point ( $X = 16.92$ ) according to (4) with the  $P^2\theta^2$  coupling.

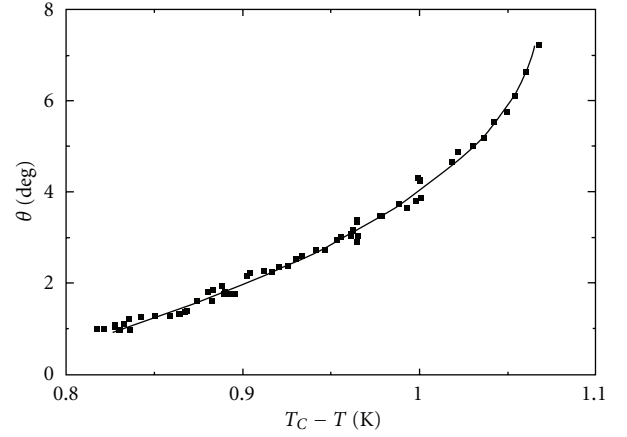


FIGURE 2: Tilt angle  $\theta$  as a function of  $T - T_C$  for the AC\* transition in a mixture of 70PDOB+C7 near the tricritical point ( $X = 16.92$ ) according to (9) with the  $P\theta + P^2\theta^2$  coupling.

fitted to the experimental data [9] and the coefficients were determined. Table 2 gives values of the coefficients with the uncertainties from (4) according to the biquadratic coupling ( $P^2\theta^2$ ) for this mixture of 70PDOB+C7 when the tricritical concentration of 70PDOB is  $X = 16.92$  for the AC\* transition. We plot  $\theta$  versus  $T - T_C$  in Figure 1. We also calculated the temperature dependence of the tilt angle  $\theta$  by fitting (9) to the experimental data [9] in the case of both biquadratic ( $P^2\theta^2$ ) and bilinear ( $P\theta$ ) couplings. Coefficients with the uncertainties and plots of  $\theta$  versus  $T - T_0$  are given in Table 2 and Figure 2, respectively.

### 4. Discussion

The tilt angle  $\theta$  was calculated as a function of temperature in the C\* phase for the AC\* transition near the tricritical concentration of 70PDOB ( $X = 16.92$ ) in C7 using the mean-field models with the  $P^2\theta^2$  (1) and  $P\theta + P^2\theta^2$  (6)

TABLE 2: Values of the parameters given in the equations indicated for the AC\* transition in a mixture of 70PDOB+C7 near the tricritical point ( $X = 16.92$ ).

$\chi_0$	$T_0$ (°C)	$a$ (J/m <sup>3</sup> K deg <sup>2</sup> )	$b$ (J/m <sup>3</sup> deg <sup>4</sup> )	$c$ (J/m <sup>3</sup> deg <sup>6</sup> )	$C$ (J/m <sup>3</sup> C deg)	$D$ (J·m/C <sup>2</sup> deg <sup>2</sup> )	$e$ (Jm <sup>5</sup> /C <sup>4</sup> )	Equation
4.59	44.668	1642.41 ± 1.30	15.41 ± 0.01	$-5.32 \times 10^{-5}$ ± $4.78 \times 10^{-8}$	—	2.546 ± 0.001	3.557 ± 0.002	(4)
4.59	44.668	$1.77 \times 10^{17}$ ± $1.7 \times 10^{14}$	$8.31 \times 10^{14}$ ± $4.6 \times 10^{12}$	$3.18 \times 10^{12}$ ± $1.13 \times 10^{11}$	$6.83 \times 10^{13}$ ± $2.6 \times 10^7$	$4.05 \times 10^6$ ± $1.4 \times 10^5$	—	(9)

couplings, as shown in Figures 1 and 2, respectively. Both equations, (4) with the  $P^2\theta^2$  coupling and (9) with the  $P\theta + P^2\theta^2$ , when fitted to the experimental data [9], describe the observed behaviour of the tilt angle  $\theta$  near the tricritical point (TCP) satisfactorily. We also calculated the standard deviations of the fitted parameters for both mean-field models, as given in Table 2. The uncertainties in the coefficients of the free energies ((1) and (6)) are comparatively small in most cases (Table 2). However, these uncertainties can be significant for the coefficients in the free energies for both models since the critical behaviour of the mesomorphic mixture depends on those coefficients, in particular the coefficients of the coupling terms ( $DP^2\theta^2$  and  $CP\theta$ ). For the mesomorphic mixture studied here, regarding the values of  $C$  and  $D$  (Table 2) for the second mean-field model (6), the bilinear  $P\theta$  coupling is dominant in comparison with the biquadratic coupling  $P^2\theta^2$ . However, considering all the values of the fitted parameters in the free energy expansion (Table 1), the mean-field model with the  $P^2\theta^2$  coupling (1) can still be preferred since (4) provides the values of the fitted parameters which are physically meaningful. This then indicates that the dominant mechanism of the smectic AC\* transition near the tricritical point is due to quadratic interactions for a mixture of 70PDOP+C7. In (1) the biquadratic coupling terms ( $P^2\theta^2$ ) characterizes the nonchiral properties and induces a transverse quadrupolar ordering. This is the dominant term in a wide temperature range far away from  $T_C$ . To stabilize the mesomorphic mixture for far away  $T_C$ , we included the  $P^4$  term, which has also been considered in the generalized mean-field model for the smectic A-chiral-smectic C phase transition in the case of p-(n-decyloxybenzylidene)-p-amino-(2-methylbutyl) cinnamate (DOBAMBC) in an earlier study [3]. Since the bilinear coupling term ( $P\theta$ ) characterizes the chiral properties close to the  $T_C$ , the mesomorphic mixture is already stabilized with the biquadratic coupling term ( $P^2\theta^2$ ) and, no additional term such as  $P^4$  is required, in (6). So that the free energy of the smectic C\* phase is given in terms of the spontaneous polarization up to  $P^2$  with the bilinear coupling term  $P\theta I$  as also given previously [3] and with this free energy the system is stable. Thus, the temperature dependence of  $\theta$  is for both mean-field models studied here. In fact the case of DOBAMBC, the relative importance of biquadratic term  $P^2\theta^2$  and  $P^4$  term in comparison with terms involving  $P\theta$  and  $P^2$  has been demonstrated numerically using the generalized mean-field model for the AC\* transition [3, Table III]. Thus, as explained previously [3], when relatively reliable experimental data is obtained in the temperature

range studied, the biquadratic term  $P^2\theta^2$  and  $P^4$  are not negligible as we also demonstrate in our study here (Table 2). Thus, the terms  $\theta^6$ ,  $P^2\theta^2$ ,  $\theta^4$ , and  $P^4$  (1), and  $P^2\theta^2$ ,  $P\theta$ , and  $P^2$  (6) are required to explain the major features of the AC\* transition in C7-70PDOB. We also note that from the data analysis point of view, if the  $P^4$  term was added to the free energy of the C\* phase (6), the fitting of the model to the experimental data would not have been a straightforward problem. This is due to the  $P^3$  term appearing in (7) when the free energy was minimized with respect to the polarization  $P$ . As a cubic polarization equation, two solutions would correspond to a local minimum of the free energy, which may then incorporate the thermal fluctuations in the mean-field model, as also pointed out previously [14].

The temperature dependence of the tilt angle  $\theta$  was calculated here near the tricritical point ( $X = 16.92$ ) using the experimental data [9] where they obtained  $\beta = 0.436$  according to a power-law formula

$$\phi = \phi_0 \left[ \frac{T_{AC^*} - T}{T_{AC^*}} \right]^\beta. \quad (10)$$

In (10)  $\phi$  is the tilt angle,  $\phi_0$  is the amplitude,  $T_{AC^*}$  is the AC\* transition temperature, and  $\beta$  is the critical exponent for the order parameter [26]. The experimental tilt-angle data were analyzed within the temperature interval of 240 mK for  $X = 16.92$  mixture of 70PDOB in C7 [9]. The experimental tilt-angle ( $\phi$ ) data were also the same as those obtained from the analyses within the temperature intervals of 103 mK ( $\beta = 0.5$ ), 490 mK ( $\beta = 0.38$ ), and 930 mK ( $\beta = 0.343$ ) [9]. Similarly, the temperature dependence of the tilt angle can also be calculated for the AC\* transition in a mixture of 70PDOB-C7 in the case of various concentrations of 70PDOB on the basis of our mean-field models given here. Since the tilt angle  $\phi$  has been obtained from the layer spacing data as a function of  $T_{AC^*} - T$  for C7 and its mixture with 70PDOB for concentrations of 0 (C7), 5.15, 9.68, 15.0, and 19.4 [8], (4) and (9) can be fitted to those data to describe the AC\* transition in this mixture. Since  $X = 0$  corresponds to a first-order AC\* transition in C7, as the concentration of 70PDOB increases towards  $X = 19.4$ , the AC\* transition then becomes a second order through  $X = 16.92$  (tricritical transition) for this mixture of 70PDOB-C7. Thus, from a first order to a second order via the tricritical point (TCP) AC\* transition, as the concentration (70PDOB) increases, can be described adequately by calculating the temperature dependence of the tilt angle using the experimental data [9] on the basis of our mean-field models studied. Mean-field to

tricritical crossover behaviour near the AC\* tricritical point can then be better understood for a mixture of 70PDOB-C7. This work is under progress.

## 5. Conclusions

The tilt angle was predicted as a function of temperature for the AC\* transition of a mixture of 70PDOB-C7 close to the tricritical point. The mean-field models which consider the quadratic and dipolar interactions between the tilt angle and the spontaneous polarization were used for this calculation of the tilt angle. Expressions for tilt angle which we derived from our mean-field models were fitted to the experimental data and the coefficients were determined.

Our results show that quadratic interactions seem to be dominant in the mechanism of the AC\* transition for the 70PDOB-C7 mixture near the tricritical point in regard to the experimental data.

## References

- [1] P. G. de Gennes, "Some remarks on the polymorphism of smectics," *Molecular Crystals and Liquid Crystals*, vol. 21, no. 1-2, pp. 49–76, 1973.
- [2] C. C. Huang and J. M. Viner, "Nature of the smectic-A-smectic-C phase transition in liquid crystals," *Physical Review A*, vol. 25, no. 6, pp. 3385–3388, 1982.
- [3] C. C. Huang and S. Dumrangrattana, "Generalized mean-field model for the smectic-A-chiral-smectic-C phase transition," *Physical Review A*, vol. 34, no. 6, pp. 5020–5026, 1986.
- [4] T. Chan, Ch. Bahr, G. Heppke, and C. W. Garland, "Landau second order to tricritical crossover behaviour for smectic A-smectic C\* transitions," *Liquid Crystals*, vol. 13, no. 5, pp. 667–675, 1993.
- [5] F. Yang, G. W. Bradberry, and J. R. Sambles, "Optical confirmation of the extended mean-field theory for a smectic-C\*-smectic-A transition," *Physical Review E*, vol. 50, no. 4, pp. 2834–2838, 1994.
- [6] F. Mercuri, M. Marinelli, U. Zammit, C. C. Huang, and D. Finotello, "Critical behavior of thermal parameters at the smectic-A-hexatic-B and smectic-A-smectic-C phase transitions in liquid crystals," *Physical Review E*, vol. 68, Article ID 051705, 10 pages, 2003.
- [7] K. Denolf, B. Van Roie, G. Pitsi, and J. Thoen, "Investigation of the smectic-A-smectic-C\* transition in liquid crystals by adiabatic scanning calorimetry," *Molecular Crystals and Liquid Crystals*, vol. 449, no. 1, pp. 47–55, 2006.
- [8] B. R. Ratna, R. Shashidhar, G. G. Nair, S. K. Prasad, Ch. Bahr, and G. Heppke, "Evidence of a first-order smectic-smectic-C\* transition and its approach to tricritical behavior," *Physical Review A*, vol. 37, no. 5, pp. 1824–1826, 1988.
- [9] R. Shashidhar, B. R. Ratna, G. G. Nair, S. K. Prasad, Ch. Bahr, and G. Heppke, "Mean-field to tricritical crossover behavior near the smectic-A-smectic-C\* tricritical point," *Physical Review Letters*, vol. 61, no. 5, pp. 547–549, 1988.
- [10] H. Y. Liu, C. C. Huang, Ch. Bahr, and G. Heppke, "Tricriticality near the smectic-A-smectic-C transition of a liquid-crystal compound," *Physical Review Letters*, vol. 61, no. 3, pp. 345–348, 1988.
- [11] Ch. Bahr and G. Heppke, "Influence of electric field on a first-order smectic-A-ferroelectric-smectic-C liquid-crystal phase transition: a field-induced critical point," *Physical Review A*, vol. 41, no. 8, pp. 4335–4342, 1990.
- [12] Ch. Bahr and G. Heppke, "Critical exponents of the electric-field-induced smectic-A-ferroelectric-smectic-C liquid-crystal critical point," *Physical Review A*, vol. 44, no. 6, pp. 3669–3672, 1991.
- [13] J. Zubia, M. Castro, J. A. Puertolas, J. Etxebarria, M. A. P. Jubindo, and M. R. de la Fuente, "Character of the smectic-A-chiral-smectic-C phase transition near a chiral-nematic-smectic-A-chiral-smectic-C point," *Physical Review E*, vol. 48, no. 3, pp. 1970–1976, 1993.
- [14] T. Carlsson, B. Zeks, A. Levstik, C. Filipic, I. Levstik, and R. Blinc, "Generalized Landau model of ferroelectric liquid crystals," *Physical Review A*, vol. 36, no. 3, pp. 1484–1487, 1987.
- [15] P. K. Mukherjee, "Tricritical behavior of the smectic-A to smectic-C\* transition," *Journal of Chemical Physics*, vol. 131, no. 7, Article ID 074902, 2009.
- [16] H. Yurtseven and M. Kurt, "Tilt angle and the temperature shifts calculated as a function of concentration for the AC\* phase transition in a binary mixture of liquid crystals," *International Journal of Modern Physics B*, vol. 25, no. 13, pp. 1791–1806, 2011.
- [17] H. Yurtseven and M. Kurt, "Spontaneous polarization and the tilt angle as a function of temperature in chiral smectic C phase of SCE9 and SCE10," *Balkan Physics Letters*, vol. 19, no. 191039, Article ID 19 191039, pp. 335–340, 2011.
- [18] H. Yurtseven and M. Kurt, "Temperature dependence of the order parameters (spontaneous polarization and the tilt angle) at various concentrations for a mixture of SCE9 + SCE10," *Liquid Crystals*, vol. 39, no. 5, pp. 539–544, 2012.
- [19] S. Salihoglu, H. Yurtseven, A. Giz, D. Kayışoglu, and A. Konu, "The mean field model with  $P^2\theta^2$  coupling for the smectic A-smectic C\* phase transition in liquid crystals," *Phase Transitions*, vol. 66, no. 1–4, pp. 259–270, 1998.
- [20] S. Salihoglu, H. Yurtseven, and B. Bumin, "Concentration dependence of polarization for the AC\* phase transition in a binary mixture of liquid crystals," *International Journal of Modern Physics B*, vol. 12, no. 20, pp. 2083–2090, 1998.
- [21] H. Yurtseven and E. Kilit, "Critical behaviour of the dielectric constant for the smectic AC\* transition under the electric field in ferroelectric liquid crystals," *Physics and Chemistry of Liquids*, vol. 50, no. 3, pp. 367–377, 2012.
- [22] H. Yurtseven and H. Karacali, "Calculation of a generalised smectic-hexatic phase diagram in liquid crystals," *Physics and Chemistry of Liquids*, vol. 50, no. 3, pp. 302–315, 2012.
- [23] R. Brout, *Phase Transitions*, chapter 2, Benjamin, New York, NY, USA, 1965.
- [24] Ch. Bahr, G. Heppke, and N. K. Sharma, "Dielectric studies of the smectic C\*-smectic A transition of a ferroelectric liquid crystal with high spontaneous polarization," *Ferroelectrics*, vol. 76, no. 1, pp. 151–157, 1987.
- [25] Z. Kutnjak and C. W. Garland, "Generalized smectic-hexatic phase diagram," *Physical Review E*, vol. 57, no. 3, pp. 3015–3020, 1998.
- [26] L. Martinez-Miranda, A. R. Kortan, and R. J. Birgeneau, "Phase diagram, fluctuations, and phase transitions near the liquid-crystal nematic-smectic-A-smectic-C multicritical point," *Physical Review A*, vol. 36, no. 5, pp. 2372–2383, 1987.

## Research Article

# Calculation of the Dielectric Constant as a Function of Temperature Close to the Smectic A-Smectic B Transition in B5 Using the Mean Field Model

Hamit Yurtseven<sup>1</sup> and Emel Kilit<sup>2</sup>

<sup>1</sup>Department of Physics, Middle East Technical University, 06531 Ankara, Turkey

<sup>2</sup>Department of Physics, Yuzuncu Yil University, 65080 Van, Turkey

Correspondence should be addressed to Hamit Yurtseven, hamit@metu.edu.tr

Received 4 July 2012; Revised 24 September 2012; Accepted 25 September 2012

Academic Editor: Durga Ojha

Copyright © 2012 H. Yurtseven and E. Kilit. This is an open access article distributed under the Creative Commons Attribution License, which permits unrestricted use, distribution, and reproduction in any medium, provided the original work is properly cited.

The temperature dependence of the static dielectric constant ( $\epsilon$ ) is calculated close to the smectic A-smectic B ( $S_A$ - $S_B$ ) transition ( $T_c = 71.3^\circ\text{C}$ ) for the liquid crystal compound B5. By expanding the free energy in terms of the order parameter in the mean field theory, the expression for the dielectric susceptibility (dielectric constant) is derived and is fitted to the experimental data for  $\epsilon$  which was obtained at the field strengths of 0 and 67 kV/cm from literature. Coefficients in the free energy expansion are determined from our fit for the  $S_A$ - $S_B$  transition of B5. Our results show that the observed behaviour of the dielectric constant  $\epsilon$  close to the  $S_A$ - $S_B$  transition in B5 can be described satisfactorily by our mean field model.

## 1. Introduction

Various smectic phases which occur in ferroelectric liquid crystals are of interest to study close to the phase transitions. In the smectic A phase, the long axes of the liquid crystal molecules are parallel to the director which is perpendicular to the smectic layers. In the smectic C (or  $C^*$ ) phase, those molecules are tilted (a tilt angle  $\theta$  between the long axis and the director) and in the presence of the chiral molecules, the AC (or  $AC^*$ ) transition becomes more interesting to study in ferroelectric liquid crystals. As in the smectic C (or  $C^*$ ) phase, the molecules are tilted in the smectic G phase and it has been observed experimentally [1] that the transitions between the ferroelectric phases (smectic A-C, smectic A-G and smectic C-G) are influenced by an applied electric field. However, it has also been observed [1] that transitions between the nonferroelectric phases (smectic A-B, smectic B-E) are not influenced by an applied electric field. This has been demonstrated experimentally [1] for the nonferroelectric phases of smectic A, B, and E of compound B5 by measuring the temperature dependence of the dielectric constant at fixed field strengths.

Some theoretical models have been given in the literature to explain the transitions between the smectic phases. The mean field models where the free energy is expanded in terms of the order parameters with the coupling terms, have been used to analyze the experimental data. Regarding the spontaneous polarization  $P$  and the tilt angle  $\theta$ , a bilinear coupling ( $P\theta$ ) [1, 2] and biquadratic coupling ( $P^2\theta^2$ ) [3–5] in the free energy expansion have been used in the mean field models for the smectic AC (or  $AC^*$ ) transitions. In our earlier studies [6–10], we have also studied the mean field models with the  $P^2\theta^2$  and  $P\theta$  couplings for the AC (or  $AC^*$ ) transitions in ferroelectric liquid crystals.

In this study, we focus on the smectic A-B transition in compound B5 and we analyze the experimental data [1] for the temperature dependence of the dielectric constant  $\epsilon$  for constant electric fields of 0 and 67 kV/cm. For this analysis, we use our mean field model [6] with the biquadratic coupling between the order parameters (polarization  $P$ ) and a long-range bond-orientational order [11] for the smectic A-smectic B transition in B5.

Below, in Section 2 we give our mean field model for the smectic A-B transition. In Section 3, our calculations and

results are given. We discuss our results in Section 4 and finally, conclusions are given in Section 5.

## 2. Theory

The smectic A-smectic B transition can be described by the free energy expanded in terms of the two-order parameters, namely, polarization  $P$  (smectic A and B phases) and a long-range bond-orientational order  $\psi$  (smectic B phase only) under an external electric field. Thus, the free energy can be written as

$$g = \frac{1}{2}\alpha\psi^2 + \frac{1}{4}b\psi^4 + \frac{1}{6}c\psi^6 + \frac{1}{2\chi_0\epsilon_0}P^2 - DP^2\psi^2 + \frac{1}{4}eP^4. \quad (1)$$

Here,  $\alpha = a(T - T_c)$  where  $T_c$  is the transition temperature between the smectic A and B phases,  $\chi_0$  is a constant dielectric susceptibility, and  $\epsilon_0$  is the permittivity.  $a$ ,  $b$ ,  $c$ , and  $e$  are constants and  $D$  is the coupling constant in (1).

The temperature dependence of the polarization  $P$  and the bond-orientational order  $\psi$  can be obtained from the minimization of the free energy (1) with respect to  $P$  and  $\psi$ , which gives

$$\alpha + b\psi^2 + c\psi^4 - 2DP^2 = 0, \quad (2)$$

$$\frac{1}{\chi_0\epsilon_0} - 2D\psi^2 + eP^2 = 0, \quad (3)$$

respectively. Substituting (3) for  $P^2$  into (2) then gives the free energy  $g$  in terms of the bond-orientational order parameter  $\psi$  only,

$$g = \frac{1}{2}\alpha'\psi^2 + \frac{1}{4}b'\psi^4 + \frac{1}{6}c'\psi^6 \quad (4)$$

with the new variables

$$\alpha' = \alpha + \frac{2D}{e\chi_0\epsilon_0}, \quad b' = b - \frac{4D^2}{e}, \quad c' = c. \quad (5)$$

Since (4) gives the free energy of the smectic B phase (in terms of the bond-orientational order parameter in this phase), the dielectric susceptibility  $\chi_\psi$  can be obtained as a function of temperature by taking the second derivative of  $g$  with respect to the  $\psi$ , which gives

$$\chi_\psi^{-1} = a(T - T_c) + \frac{2D}{e\chi_0\epsilon_0} + a_1\psi^2 + a_2\psi^4, \quad (6)$$

where  $a_1 = 3b'$  (5) and  $a_2 = 5c'$ .

In order to predict the temperature dependence of the reciprocal dielectric susceptibility  $\chi_\psi^{-1}$  (6), a functional form of  $\psi$  is needed, which can be adopted from the molecular field theory [12] as follows:

$$\begin{aligned} \psi &\approx 1 - 2 \exp\left(-\frac{2T_c}{T}\right), & T \ll T_c, \\ \psi &\approx \left[3\left(1 - \frac{T}{T_c}\right)\right]^{1/2}, & 0 < T_c - T \ll T_c, \\ \psi &\approx 0, & T_c < T \end{aligned} \quad (7)$$

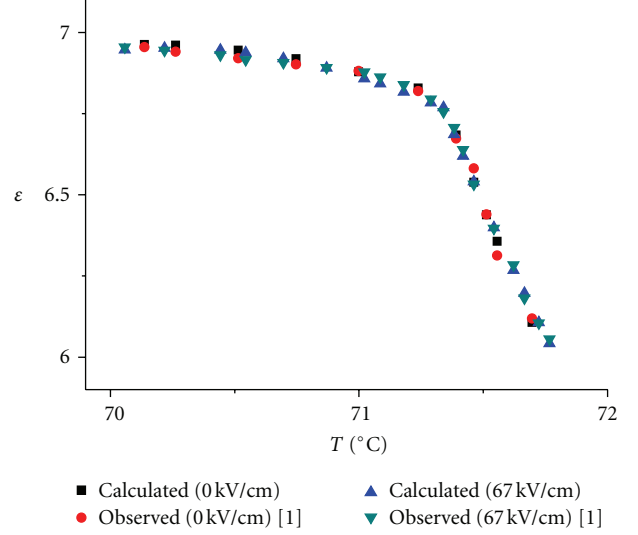


FIGURE 1: The dielectric constant  $\epsilon$  calculated from (6) as a function of temperature for the smectic A-smectic B transition under the dielectric fields of 0 and 67 kV/cm for compound B5. The observed data [1] is also shown here.

for the long-range bond-orientational order parameter in the smectic B phase. Close to the smectic A-smectic B transition, a power law formula is valid, as given in (7).

## 3. Calculations and Results

We analyzed the temperature dependence of the dielectric susceptibility according to (6) which was fitted to the experimental data for the dielectric constant  $\epsilon$  [1] ( $\chi = \epsilon - 1$ ) close to the smectic A-smectic B transition in B5. In (6), we first calculated the temperature dependence of the order parameter  $\psi$  using the power-law formula (7) where the temperature for the smectic A-smectic B transition was taken as  $T_c = 71.3^\circ\text{C}$  at zero electric field ( $E = 0$ ) in B5. By fitting (6) to the experimental  $\epsilon$  data [1], the fitted parameters  $a$ ,  $a_1$  and  $a_2$  below  $T_c$  were obtained ( $E = 0$ ), as given in Table 1. Similarly, (6) was fitted to the experimental  $\epsilon$  data [1] for the electric field of 67 kV/cm close to the smectic A-smectic B transition with the fitted parameters (Table 1). Values of  $2D/e\chi_0\epsilon_0$  were deduced from the experimental  $\epsilon$  data [1] when  $\psi = 0$  at  $T = T_c$  (6). Since the transition temperatures are not induced by the external electric field for nonferroelectric phases [1], we took the same transition temperature ( $T_c = 71.3^\circ\text{C}$ ) for 67 kV/cm in B5, as shown in Figure 1. Thus, we get the same fits (6) for the fixed bias field strengths of 0 and 67 kV/cm for the smectic A-smectic B transition in B5 (Figure 1). In the same manner, we analyzed the experimental data for the dielectric constant  $\epsilon$  [1] according to (1) with  $\psi = 0$  for  $T > T_c$  using the fixed electric fields of 0 and 67 kV/cm. Values of the fitted parameter  $a$  are given within the temperature intervals in Table 2. This data is also plotted in Figure 1 with the observed data [1].

TABLE 1: Values of the coefficients according to (6) for the smectic A-smectic B transition below  $T_c$  within the temperature interval under the electric fields indicated for compound B5.

$E$ (kV/cm)	$T_c$ ( $^{\circ}\text{C}$ )	$a$ ( $^{\circ}\text{C}^{-1}$ )	$a_1$	$a_2$	$2D/e\chi_0\epsilon_0$	Temperature interval ( $^{\circ}\text{C}$ )
0	71.3	0.056	1.16	1.70	0.172	$70.14 < T < 71.24$
67	71.3	0.057	1.13	2.53	0.173	$70.06 < T < 71.29$

TABLE 2: Values of the coefficients according to (6) for the smectic A-smectic B transition above  $T_c$  within the temperature interval under the electric fields indicated for compound B5.

$E$ (kV/cm)	$T_c$ ( $^{\circ}\text{C}$ )	$a$ ( $^{\circ}\text{C}^{-1}$ )	$2D/e\chi_0\epsilon_0$	Temperature interval ( $^{\circ}\text{C}$ )
0	71.3	0.065	0.170	$71.39 < T < 71.70$
67	71.3	0.059	0.171	$71.34 < T < 71.77$

## 4. Discussion

We analyzed here the temperature dependence of the dielectric constant  $\epsilon$  through the reciprocal dielectric susceptibility  $\chi^{-1}$  (6) in our mean field model with the biquadratic ( $P^2\psi^2$ ) coupling for the smectic A-smectic B transition in B5. As pointed out previously, transition temperatures are not shifted for the external electric fields of 0 and 67 kV/cm (Figure 1) due to the fact that the smectic A and smectic B phases are nonferroelectric of compound B5. For the ferroelectric transitions of smectic A-smectic C, smectic A-smectic G and smectic C-smectic G of compound A6, it has been observed experimentally [1] that the transition temperatures are shifted under various fixed field strengths. It has also been observed [1] that nonferroelectric phases (smectic B-smectic E) are not influenced by an electric field for this compound B5 studied here. Regarding nonferroelectric phases, in fact the smectic A phase at high temperatures occurs at zero electric field only since the external electric field induces a tilt angle which exists in the smectic C phase. The tilted smectic phase possesses a spontaneous electric polarization  $P_s$  if the molecules have a permanent dipole moment and they are chiral [13].

As shown in Figure 1, dielectric constant  $\epsilon$  increases abruptly with the decreasing temperature near the smectic A-smectic B transition ( $T_c = 71.3^{\circ}\text{C}$ ) of compound B5. This is due to the larger electroclinic effect in the smectic B phase [1].

As we pointed out previously, the dielectric constant (or dielectric susceptibility) was calculated as a function of temperature (6) from our mean field model with the biquadratic  $P^2\psi^2$  coupling (1) for the smectic A-smectic B transition of compound B5 (Figure 1). In this model, the long-range bond-orientational order parameter  $\psi$  was considered as the primary order parameter and the polarization  $P$  as the secondary order parameter in the free energy expansion (1). With the biquadratic coupling ( $P^2\psi^2$ ), quadrupolar interactions between the molecules are attributed to the mechanism of the smectic A-smectic B transition of compound B5 in our mean field model. Regarding the temperature dependence of the dielectric constant  $\epsilon$  calculated from (6) which was fitted to the experimental data [1] as stated above, our mean field model describes the observed behaviour of  $\epsilon$  satisfactorily for the smectic A-smectic B transition of compound B5.

This indicates that the main mechanism for this transition is due to quadrupole-quadrupole interactions which involve a long-range bond-orientational ordering in B5.

## 5. Conclusions

The dielectric constant  $\epsilon$  was predicted using our mean field model with the biquadratic coupling  $P^2\psi^2$  ( $P$  is the polarization and the  $\psi$  is the long-range bond-orientational order parameter) for the smectic A-smectic B transition for constant electric fields in compound B5. The predicted  $\epsilon$  was fitted to the experimental data from the literature and the fitted parameters were determined for the smectic A-smectic B transition of compound B5. It was shown here that our mean field model describes the observed behaviour of the dielectric constant adequately for this transition of the liquid crystalline material studied here. The observed data also shows that the transition temperatures are not shifted under the electric field for this nonferroelectric transition.

## References

- [1] Ch. Bahr, G. Heppke, and B. Sabaschus, "Influence of an electric field on phase transitions in ferroelectric liquid crystals," *Liquid Crystals*, vol. 11, no. 1, pp. 41–48, 1992.
- [2] Ch. Bahr and G. Heppke, "Influence of electric field on a first-order smectic-A-ferroelectric-smectic-C liquid-crystal phase transition: a field-induced critical point," *Physical Review A*, vol. 41, pp. 4335–4342, 1990.
- [3] C. C. Huang and S. Dumrongrattana, "Generalized mean-field model for the smectic-A chiral-smectic C phase transition," *Physical Review A*, vol. 34, no. 6, pp. 5020–5026, 1986.
- [4] T. Carlsson, B. Zeks, A. Levstik, C. Filipic, I. Levstik, and R. Blinc, "Generalized Landau model of ferroelectric liquid crystals," *Physical Review A*, vol. 36, no. 3, pp. 1484–1487, 1987.
- [5] R. Blinc, "Models for phase transitions in ferroelectric liquid crystals: theory and experimental results," in *Phase Transitions in Liquid Crystals*, S. Martellucci and A. N. Chester, Eds., Plenum Press, New York, NY, USA, 1992.
- [6] S. Salihoğlu, H. Yurtseven, A. Giz, D. Kayışoğlu, and A. Konu, "The mean field model with  $P^2\theta^2$  coupling for the smectic A-smectic C\* phase transition in liquid crystals," *Phase Transitions*, vol. 66, pp. 259–270, 1998.

- [7] S. Salihođlu, H. Yurtseven, and B. Bumin, "Concentration dependence of polarization for the AC\* phase transition in a binary mixture of liquid crystals," *International Journal of Modern Physics B*, vol. 12, no. 20, pp. 2083–2090, 1998.
- [8] H. Yurtseven and E. Kilit, "Temperature dependence of the polarization and tilt angle under an electric field close to the smectic AC\* phase transition in a ferroelectric liquid crystal," *Ferroelectrics*, vol. 365, no. 1, pp. 122–129, 2008.
- [9] E. Kilit and H. Yurtseven, "Calculation of the dielectric constant as a function of temperature near the smectic AC\* phase transition in ferroelectric liquid crystals," *Ferroelectrics*, vol. 365, no. 1, pp. 130–138, 2008.
- [10] H. Yurtseven and M. Kurt, "Tilt angle and the temperature shifts calculated as a function of concentration for the AC\* phase transition in a binary mixture of liquid crystals," *International Journal of Modern Physics B*, vol. 25, no. 13, pp. 1791–1806, 2011.
- [11] Z. Kutnjak and C. W. Garland, "Generalized smectic-hexatic phase diagram," *Physical Review E*, vol. 57, no. 3, pp. 3015–3020, 1998.
- [12] R. Brout, *Phase Transitions*, chapter 2, Benjamin, New York, NY, USA, 1965.
- [13] R. B. Meyer, L. Liebert, L. Strzelecki, and P. Keller, "Ferroelectric liquid crystals," *Journal de Physique Lettres*, vol. 36, no. 3, pp. 69–71, 1975.

## Research Article

# Liquid Crystal Thermography Measurement Uncertainty Analysis and Its Application to Turbulent Heat Transfer Measurements

Yu Rao<sup>1</sup> and Yamin Xu<sup>2</sup>

<sup>1</sup> School of Mechanical and Power Engineering, Shanghai Jiaotong University, 800 Dongchuan Road, Shanghai 200240, China

<sup>2</sup> School of Aeronautics and Astronautics, Shanghai Jiaotong University, 800 Dongchuan Road, Shanghai 200240, China

Correspondence should be addressed to Yamin Xu, xuyam\_2003@163.com

Received 13 July 2012; Accepted 27 August 2012

Academic Editor: Durga Ojha

Copyright © 2012 Y. Rao and Y. Xu. This is an open access article distributed under the Creative Commons Attribution License, which permits unrestricted use, distribution, and reproduction in any medium, provided the original work is properly cited.

Liquid crystal thermography is an advanced nonintrusive measurement technique, which is capable of providing a high-accuracy continuous temperature field measurement, especially for a complex structured heat transfer surface. The first part of the paper presents a comprehensive introduction to the thermochromic liquid crystal material and the related liquid crystal thermography technique. Then, based on the authors' experiences in using the liquid crystal thermography for the heat transfer measurement, the parameters affecting the measurement uncertainty of the liquid crystal thermography have been discussed in detail through an experimental study. The final part of the paper describes the applications of the steady and transient liquid crystal thermography technique in the study of the turbulent flow heat transfer related to the aeroengine turbine blade cooling.

## 1. Introduction

Thermochromic liquid crystal (TLC) is a cholesteric liquid crystal material. The cholesteric materials form a similar structure; however, under different temperatures the orientations of adjacent liquid crystal molecule planes are different with certain angles, which results in the reflection of different wavelengths of the visible spectrum of light when illuminated with white light and then show different colors [1–3]. Such optical characteristics of the TLC depend on its temperature and are repeatable and reversible. The accurate relations between the TLC colors and temperatures can be built through careful calibration experiments, which then can be used for precise temperature measurements of any surface.

Currently, the TLC can be provided with the operating temperature between  $-30^{\circ}\text{C}$  and  $150^{\circ}\text{C}$ . The TLC may have the bandwidth (the active temperature range) of  $1^{\circ}\text{C}$  to  $20^{\circ}\text{C}$ , in which the liquid crystal can be applied for the temperature measurements by changing color: smoothly from red to blue. The response time of TLC is about 3 ms [3]. Pure TLC materials are organic compounds that can easily degrade when exposed to chemical contamination and to ultraviolet (UV) light. Currently, people can use microencapsulation process to reduce the degradation. The microsized TLC particles

are microencapsulated within transparent polymer shells (PMMA), which can significantly improve the stability of liquid crystal materials and make them capable of being handled easily. The TLC materials are currently supplied by the Hallcrest Ltd. (Glenview, USA) and Merck Ltd. (Pool, UK).

TLC thermography, as a powerful nonintrusive optical technique for temperature measurement, is capable of providing a high-accuracy continuous temperature field measurement, especially for a complex structured heat transfer surface [3, 4]. However, before the TLC is used for the temperature measurement, the hue-temperature calibration must be conducted. In the past two decades, many studies have been conducted on the calibration methods of the TLC. Rao and Zang [2], Camci et al. [5], Farina et al. [6], Behle et al. [7], Sabatino et al. [8], and Chan et al. [9] studied experimentally the effects of the lighting angles and viewing angles on the hue-temperature calibration curves of the TLCs. Roth and Anderson [10], Wiberg and Lior [11], Abdullah et al. [12], and Rao et al. [13] studied experimentally the effects of the coating thickness on the TLC hue-temperature calibration curves. These previous researches only indicated that the lighting angle and the coating thickness can significantly affect the TLC hue-temperature calibration curves. It should

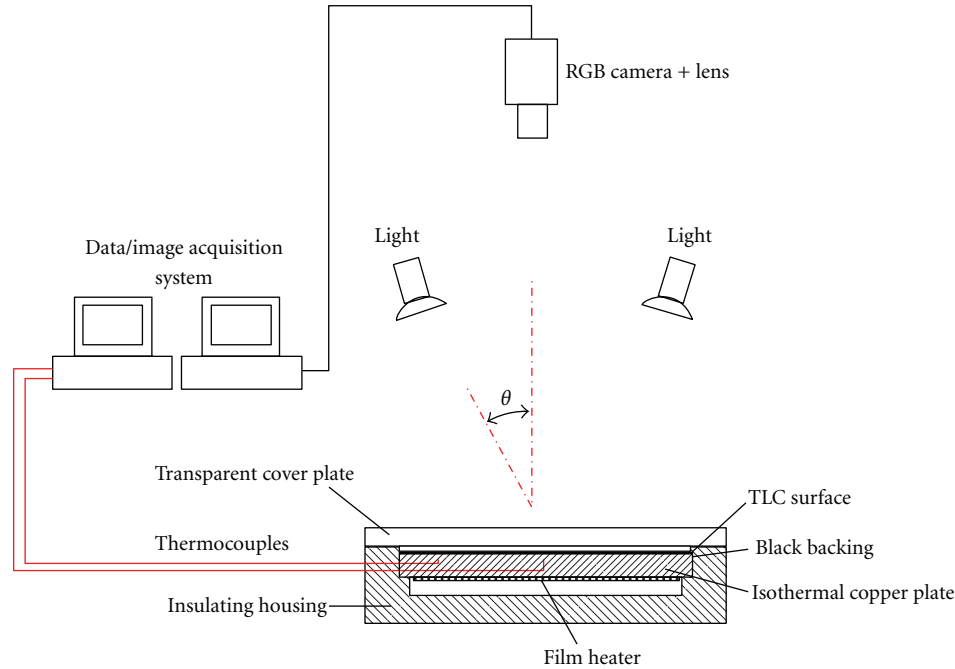


FIGURE 1: The TLC calibration experimental apparatus.

be pointed out that, though previous studies have indicated that such factors as lighting angles and coating thickness can influence the TLC hue-temperature calibration curves, reports on how the temperature measurement uncertainty of the TLC is influenced by those factors are still quite limited.

In the present paper, the first part is focused on the discussing on the effects of the measurement parameters on the measurement uncertainty of the TLC thermography, and the second part is focused on the application of the TLC thermography to the turbulent heat transfer studies.

## 2. Parametric Analysis on the Measurement Uncertainty of TLC

There are many factors that can affect the TLC thermography measurement uncertainty, such as the TLC bandwidth, the color imaging processing techniques, the coating thickness, the quality of the TLC coating, and the lighting angle, and so forth.

In order to study the effects of those parameters on the measurement uncertainty of the TLC, a calibration experimental apparatus was constructed as is shown in Figure 1. The TLC thermography system consists of a Hitachi (HV-D30P) 3CCD RGB camera with a zoom lens, cold lighting source, a data acquisition system, an image acquisition system, and the related data processing software. The calibration device consists of a transparent Plexiglas cover plate, a copper plate with a film heater, and two type K thermocouples (0.5 mm in diameter) with the measurement uncertainty of  $\pm 0.1^\circ\text{C}$ .

By adjusting the voltage over the film heater, the copper plate's surface temperature can be controlled precisely and rapidly. The surface of the copper base plate was first painted black paint and then a layer of liquid crystal (10–40  $\mu\text{m}$  in thickness). The supplied microencapsulated TLC slurry (Hallcrest SPN100R40C20W) has an operating temperature range of 40–60 $^\circ\text{C}$ . The changing color under the varying temperature is recorded by the 3CCD RGB camera. The TLC images are then processed by a self-developed data processing program, and the corresponding TLC hue-temperature relationship can be obtained. With the calibration experimental system, the authors have studied the effects of the influencing parameters on the measurement uncertainty of the TLC.

*2.1. Effect of the Bandwidth of TLC on the Measurement Uncertainty.* According to the working bandwidth, the TLC can be generally divided into the narrowband TLC and wideband TLC. A narrowband TLC has an active temperature range of 1 $^\circ\text{C}$ , and a wideband TLC can have an active temperature range of 5 $^\circ\text{C}$ , 10 $^\circ\text{C}$ , or 20 $^\circ\text{C}$ . As the bandwidth of the TLC decreases, the sensitivity of hue to temperature increases, and then the measurement accuracy of the TLC increases. The previous literatures showed that the measurement uncertainty of the narrowband TLCs is about  $\pm 0.1^\circ\text{C}$  [12],  $\pm 0.1$ – $0.3^\circ\text{C}$  [7], and  $\pm 0.2$ – $0.4^\circ\text{C}$  [8] for the TLCs with the bandwidth of 5 $^\circ\text{C}$  and 10 $^\circ\text{C}$ , respectively. The TLC with the bandwidth of 20 $^\circ\text{C}$  has the measurement uncertainty of about  $\pm 0.4$ – $0.5^\circ\text{C}$  [2].

*2.2. Effect of Image Processing on the Measurement Uncertainty.* Figure 2 shows the raw hue and the median filtered

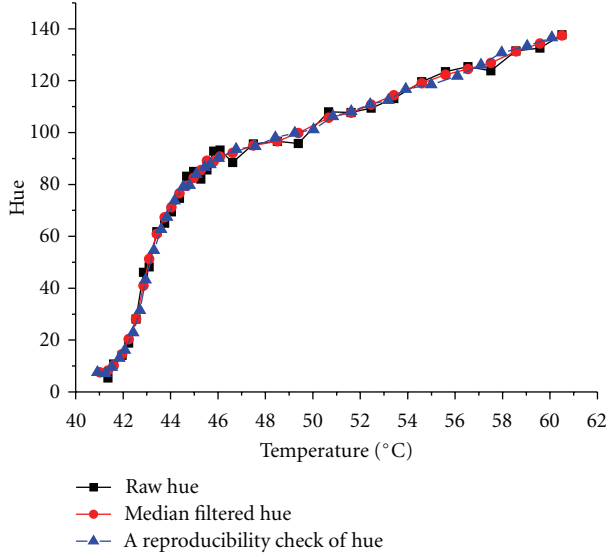


FIGURE 2: The raw hue and the median filtered hue calibrations of the TLC.

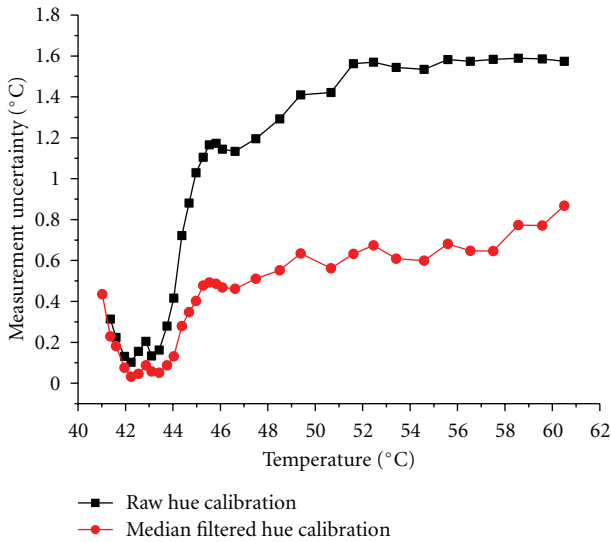


FIGURE 3: The measurement uncertainty in the raw hue and the median filtered hue calibrations.

hue calibrations of the TLC. The calibration experiment was done with the finely prepared TLC coating with a thickness of  $25\ \mu\text{m}$ , and the lighting angle is  $27^\circ$ . The hue value can be calculated by the following algorithms [14].

$$\begin{aligned} \text{If } R = \text{Max, } \text{Hue} &= \frac{G - B}{6(R - \min(R, G, B))}, \\ \text{If } G = \text{Max, } \text{Hue} &= \frac{2 + B - R}{6(G - \min(R, G, B))}, \\ \text{If } B = \text{Max, } \text{Hue} &= \frac{4 + R - G}{6(B - \min(R, G, B))}. \end{aligned} \quad (1)$$

$R$ ,  $G$ , and  $B$  are, respectively, red, green, and blue components of the liquid crystal image pixel.

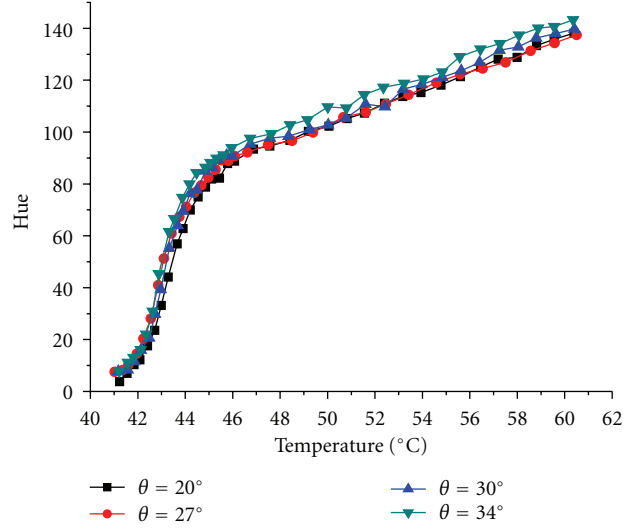


FIGURE 4: Effect of the lighting angle on the hue curve of the TLC coating.

It can be seen that the hue curve becomes much smoother than the unfiltered curve. The noise in the hue curves has been effectively removed. To check the reproducibility of the hue curve of the TLC, a second heating process was conducted. Figure 2 shows good reproducibility of the hue curve of the TLC.

To estimate the measurement uncertainty of the TLC, the method described in [8] was used. A series of constant temperature TLC color images ( $100 \times 100$  pixels) of calibration were examined. The constructed polynomial fitting of the temperature-hue relation was employed to convert each sample image to the corresponding temperature field, and the standard deviation in temperature was determined for each image. Using a 95% confidence interval, the uncertainty for each discrete temperature/image was estimated as twice the standard deviation value.

Figure 3 shows the uncertainty in temperature measurement versus the actual temperature measurement. The measurement uncertainty based on the raw hue calibration ranges from  $0.1$  to  $1.6^\circ\text{C}$  with a mean of  $0.98^\circ\text{C}$ , and the measurement uncertainty based on the median filtered hue ranges from  $0.04$  to  $0.87^\circ\text{C}$  with a mean of  $0.42^\circ\text{C}$ . Therefore, a median filtering technique can significantly improve the measurement accuracy of the TLC. It is also noteworthy that the TLC shows a region-wise measurement uncertainty distribution. Over the temperature range of  $41$ – $45^\circ\text{C}$ , due to a higher sensitivity of hue to temperature, the TLC has a higher measurement accuracy, and the median filtered hue calibration has a mean measurement uncertainty of  $0.17^\circ\text{C}$ .

**2.3. Effect of Lighting Angle on the Measurement Uncertainty.** The TLC calibration was conducted at various lighting angles of  $20^\circ$ ,  $27^\circ$ ,  $30^\circ$ , and  $34^\circ$  with the finely prepared TLC coating based on the calibration experimental system as Figure 1. Figure 4 shows the effect of the lighting angles on the hue calibration. The lighting angle has a notable effect on the

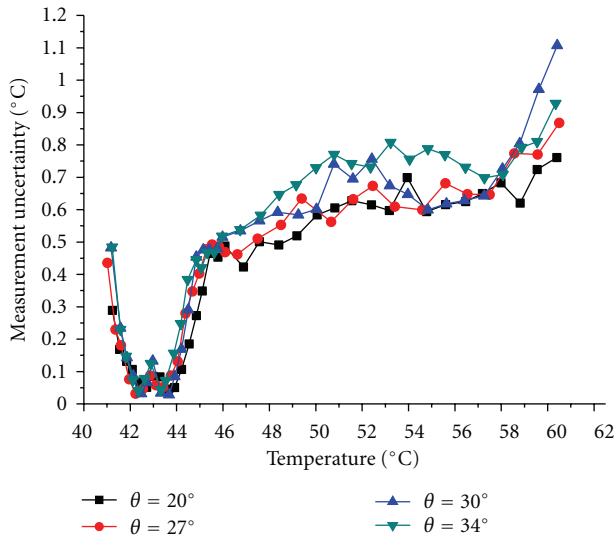


FIGURE 5: Effect of the lighting angle on the measurement uncertainty.

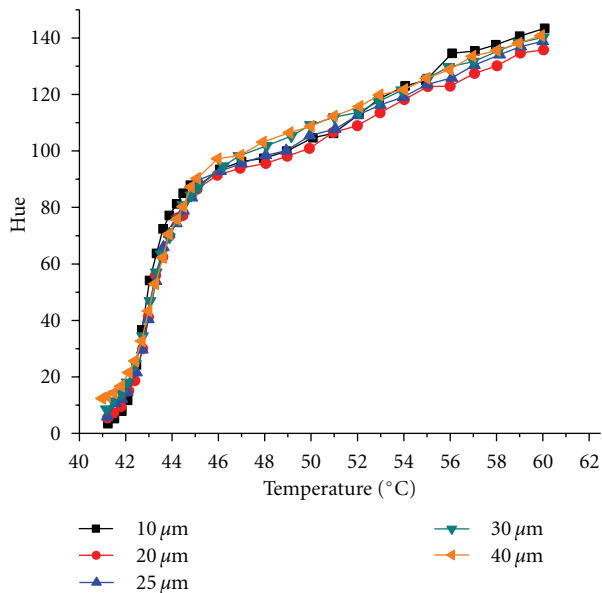


FIGURE 6: Effect of the TLC coating thickness on the hue curves.

hue-temperature curve, and as the lighting angle increases, the hue curve shifts upward.

Figure 5 shows the effect of the lighting angles on the uncertainty in temperature measurement versus the actual temperature measurement. It can be found that the measurement uncertainty increases with the lighting angle. The average measurement uncertainty with the lighting angle of  $34^\circ$  is about 25% higher than that the lighting angle of  $20^\circ$ . The reason should be that as the lighting angle decreases, the lighting intensity on the coating of the TLC is stronger, which leads to a stronger reflection of the color signal and thereby a higher measurement accuracy. The effect of the lighting angle on the measurement uncertainty is more distinctive in

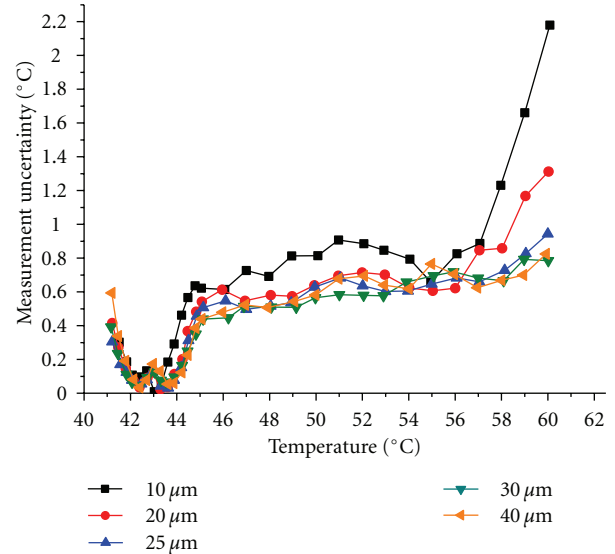


FIGURE 7: Effect of the TLC coating thickness on the measurement uncertainty.

the temperature range of  $45\text{--}60^\circ\text{C}$ , which corresponds to the region of low TLC hue sensitivity. Therefore, in order to get a higher measurement accuracy, the lighting angle should be kept as small as possible providing the experimental space and arrangements allow.

Behle et al. [7] studied the effect of lighting angle within the range of  $0\text{--}70^\circ$  on the temperature measurement uncertainty of the TLC. They have shown that the measurement uncertainty increases with the lighting angle, and the average measurement uncertainty with the lighting angle of  $35^\circ$  is about 20% higher than that with the lighting angle of  $20^\circ$ , which agrees with the experimental results in the present paper.

*2.4. Effect of TLC Coating Thickness on the Measurement Uncertainty.* The coating thickness is also an important factor affecting the TLC measurement uncertainty. Figure 6 shows the hue curves of the TLC coatings with different thickness of  $10\ \mu\text{m}$ ,  $20\ \mu\text{m}$ ,  $25\ \mu\text{m}$ ,  $30\ \mu\text{m}$ , and  $40\ \mu\text{m}$ . The lighting angle is  $27^\circ$ . It can be found that the coating thickness has a notable effect on the hue-temperature curve, and as the coating thickness increases, the hue curve shifts upward.

Figure 7 shows the effect of coating thickness on the measurement uncertainty. It can be found that, except for the TLC coating thickness of  $10\ \mu\text{m}$ , the measurement uncertainties of the other TLC coatings show similar values with a mean of about  $0.45^\circ\text{C}$  over the calibratable temperature range of  $41\text{--}60^\circ\text{C}$ , and a thicker TLC coating shows a relatively smaller measurement uncertainty. Figure 7 also indicates that the effect of the TLC coating thickness over  $20\ \mu\text{m}$  is nondistinctive on the measurement uncertainty. The TLC coating with the thickness of  $10\ \mu\text{m}$  shows a distinctively higher measurement uncertainty, which is because that the coating is very thin, leading to a weaker reflection of

the color signal and correspondingly a higher noise level in the hue.

**2.5. Effect of Coating Quality on the Measurement Uncertainty.** Due to the congregation of the micro-sized TLC particles in the slurry, the suspended congregated particles can be of relatively larger size of  $10\text{--}20\ \mu\text{m}$ . The TLC coating on the copper surface can be roughly prepared. The TLC coating can also be finely prepared by the following procedures: the TLC slurry was first diluted with an equal amount of distilled water and carefully mixed and fine-filtered; then the TLC slurry was repeatedly sprayed and dried on the black backing on the surface ( $1\text{--}5\ \mu\text{m}$  TLC particle diameters). To examine the effect of the coating quality on the TLC hue curve calibration and the measurement uncertainty, comparative calibration experiments were conducted with a roughly prepared TLC coating and a finely prepared TLC coating under the same lighting condition (the lighting angle =  $27^\circ$ ). Both coatings have the same thickness of  $25\ \mu\text{m}$ . Figure 8 shows the comparison of the hue curves of the rough coating and the fine coating. It is found that, the rough TLC coating and the fine TLC coating show different hue curves over the same monotonically calibratable temperature range. The fine TLC coating has a wider hue range, which means that the fine coating has a higher hue sensitivity to temperature and a higher resolution of the measurement.

Figure 9 shows the uncertainty in temperature measurement of the two coatings versus the actual temperature measurement. The measurement uncertainty of the fine coating ranges from  $0.04^\circ\text{C}$  to  $0.87^\circ\text{C}$  with a mean of  $0.42^\circ\text{C}$ ; however, that of the rough coating ranges from  $0.1^\circ\text{C}$  to  $1.2^\circ\text{C}$  with a mean of  $0.72^\circ\text{C}$ . The fine coating shows a considerably higher measurement accuracy than the rough coating. The reason could be that compared with the fine coating, the surface of the rough coating is much rougher, and the thickness nonuniformity produces a larger noise level. Therefore, in order to get a high measurement accuracy, a finely prepared coating should be used for the actual TLC temperature measurement application.

### 3. Application of TLC Thermography to the Turbulent Heat Transfer Measurement

**3.1. Steady and Transient TLC Thermography.** The TLC thermography is capable of providing a high-accuracy and full-field temperature measurement for structured heat transfer surfaces. Therefore, in the past 20 years the TLC thermography as a powerful tool for temperature measurement has been widely used for the turbulent heat transfer research for gas turbine/jet engine hot components' cooling design [15–20].

Specifically, the application of the TLC thermography for the turbulent heat transfer study can be categorized as steady TLC thermography technique and transient TLC thermography technique.

**3.1.1. Steady TLC Thermography Technique.** When using the steady TLC thermography technique for the heat transfer

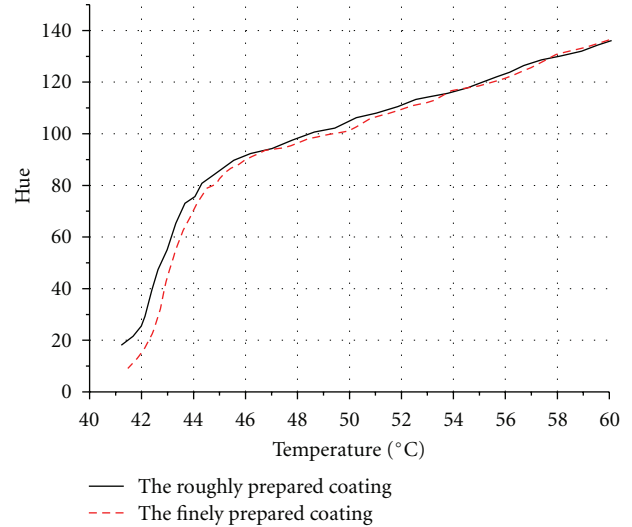


FIGURE 8: The hue curves comparison between the rough and fine TLC coatings.

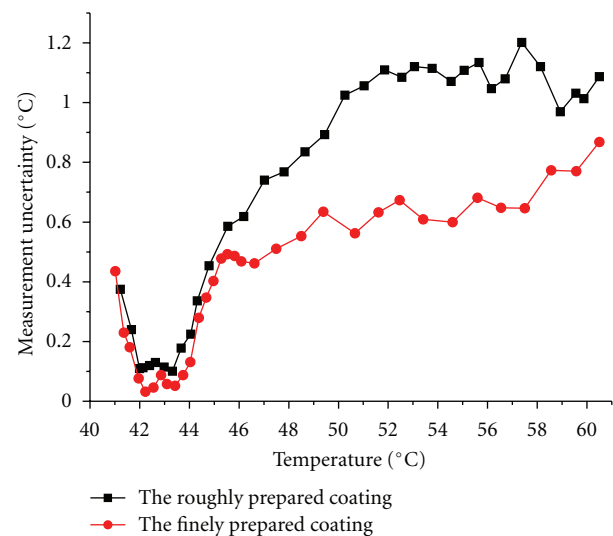


FIGURE 9: The measurement uncertainty for the rough and fine TLC coatings.

measurement, the TLC thermography usually works together with a film heater. The TLC provides the local wall temperature data, and the film heater provides a uniform surface heat flux condition, and then the heat transfer coefficient field can be obtained. However, in the situations with complex surface structures, a film heater could not be used, and then the local heat flux data should be obtained in another way. For example, in [16, 17] the heat flux data on the complex heat transfer surface with pin fins and dimples were obtained by a three-dimensional conjugate computation; by combining the temperature field obtained by the TLC thermography, the heat transfer coefficient field can then be determined.

**3.1.2. Transient TLC Thermography Technique.** The transient TLC thermography technique is an advanced and efficient

heat transfer measurement technique, which is based on the one-dimensional solution of Fourier's heat conduction equation within a semi-infinite wall [3, 18–20] and can be used to the high-accuracy heat transfer measurements in complex cooling structures.

The local wall temperature can be measured by the TLC. The local heat transfer coefficients can be determined using the measured wall temperature and the solution of the one-dimensional transient heat conduction equation for a semi-infinite solid.

The one-dimensional transient heat conduction equation is

$$k \frac{\partial^2 T}{\partial x^2} = \rho c \frac{\partial T}{\partial t}. \quad (2)$$

The boundary conditions are

$$\begin{aligned} t = 0, \quad T &= T_0, \\ x = 0, \quad -k \frac{\partial T}{\partial x} &= h(T_B - T_w), \\ x \rightarrow \infty, \quad T &= T_0, \end{aligned} \quad (3)$$

where  $T$  is the temperature,  $t$  is the time, and  $k$ ,  $\rho$  and  $c$  are the solid wall thermal conductivity, density, and specific heat, respectively. Solving (2) with the boundary conditions, the dimensionless temperature at the convective boundary wall (at  $x = 0$ ) is obtained as follows:

$$\frac{T_w - T_0}{T_B - T_0} = 1 - \exp\left(h^2 \frac{t}{k\rho c}\right) \operatorname{erfc}\left(h \sqrt{\frac{t}{k\rho c}}\right). \quad (4)$$

Equation (4) is only valid for an ideal temperature step rise within the flow. However, in reality the thermocouples record a time-dependent variation of the mainstream temperature, which can be simulated by a series of small temperature step rise. By using Duhamel's superposition theorem, the solution for the heat transfer coefficient at every location is then represented as

$$\begin{aligned} T_w - T_0 &= \sum_{i=1}^N \left[ 1 - \exp\left(h^2 \frac{(t - t_i)}{k\rho c}\right) \right. \\ &\quad \left. \times \operatorname{erfc}\left(h \sqrt{\frac{(t - t_i)}{k\rho c}}\right) \right] (T_{B,i} - T_{B,i-1}), \end{aligned} \quad (5)$$

where  $T_{B,i}$  is the airflow bulk temperature at one specific time  $t_i$ ,  $T_w$  is the measured wall temperature by the time  $t$  (indicated by the color change of the liquid crystals), and  $T_0$  is the initial wall temperature. Solving (5) by an iteration method, the heat transfer coefficient  $h$  can be determined. Since the TLC thermography can provide a full-field temperature data, therefore a full-field heat transfer coefficient data at the wall can be obtained.

**3.2. Examples of the TLC Thermography for Heat Transfer Measurements.** Pin fins and rib turbulators are the common heat transfer enhancement elements used in the gas turbine blade internal cooling channels, which produce strong

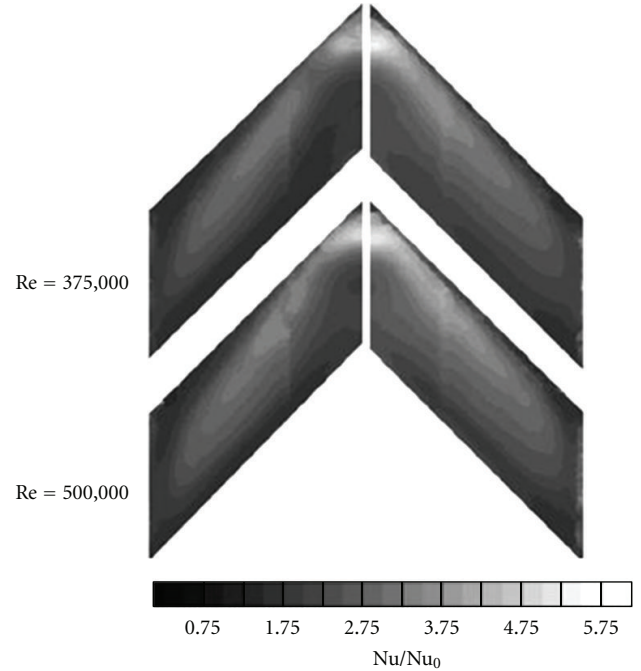


FIGURE 10: The local Nusselt number distribution on the surface with V-shaped rib turbulators [15].

turbulent flow in the cooling channels and significantly increase the convective heat transfer performance. Maurer et al. [15] studied the local heat transfer characteristics on the surface with V-shaped rib turbulators by combining the steady TLC thermography technique with the stainless steel foil heater. In their study, the local wall temperature data was obtained by the TLC thermography; a uniform heat flux condition was provided by the thin stainless steel foil heater (25  $\mu\text{m}$  thickness). Based on the local wall temperature data and the local heat flux data, the local Nusselt number distribution on the surface with V-shaped ribs was given by [15] as is shown in Figure 10. The measurement uncertainty for the heat transfer coefficient is about 12.5%. In fact, in order to achieve a uniform distribution of the heat flux at the heating surface, the thickness of the film heater should be uniform and sufficiently small, so that the transverse heat conduction effects can be neglected.

In [16, 17], the authors showed the local heat transfer characteristics on the surface with pin fins and dimples, which were obtained by combining the steady TLC thermography technique with a three-dimensional CFD computation. Figure 11 shows the experimental schematic for the pin fin-dimple channel heat transfer measurement with the steady TLC thermography. The local temperature data on the heat transfer surface were obtained by the TLC thermography, and the local wall heat flux data were determined by the three-dimensional conjugate computation. An in situ calibration on the TLC thermography has been done before the heat transfer experiments, which indicates that the TLC has the highest temperature measurement accuracy within the temperature range of 41°C–45°C. Therefore, in the convective heat transfer experiments the wall temperature

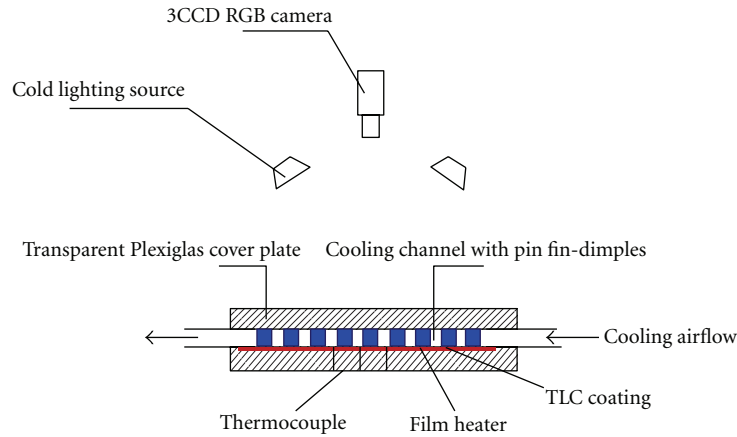


FIGURE 11: Experimental Schematic for the pin fin-dimple channel heat transfer measurement with the steady TLC thermography.

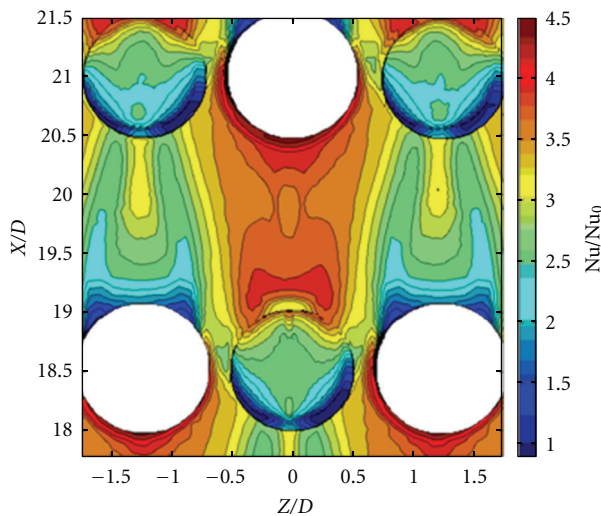


FIGURE 12: Local Nusselt number distribution on the heat transfer surface with pin fins and dimples ( $Re = 18600$ ) [16, 17].

of the pin fin-dimple plate that was carefully controlled at about  $43^{\circ}\text{C}$ . Based on the obtained local wall temperature and heat flux data, the local Nusselt number distribution on the surface with pin fin-dimple combined structures was obtained as is shown in Figure 12. The uncertainty on the heat transfer coefficient measurement is about  $\pm 6.5\%$ , and the temperature measurement uncertainty is about  $\pm 0.3^{\circ}\text{C}$ .

Schüler et al. [20] obtained the local heat transfer characteristics on the wall with angled ribs by using the transient TLC thermography technique. In their study, the air flow was heated up to  $50\text{--}60^{\circ}\text{C}$  through a mesh heater, and then flowed over a Plexiglas plate with angled ribs, which has an initial temperature of  $18^{\circ}\text{C}$ . The narrowband TLC with the bandwidth of  $1^{\circ}\text{C}$  was sprayed on surface of the Plexiglas test plate, and the duration of the transient heat transfer measurement is  $90\text{--}120\text{s}$ . Figure 13 shows the local Nusselt

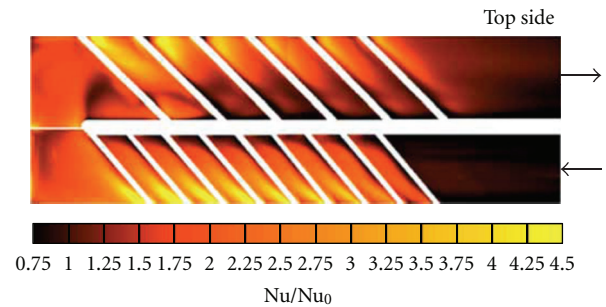


FIGURE 13: The local heat transfer characteristics on the wall with angled ribs measured by transient TLC thermography [20].

number field on the ribbed surface under turbulent flow condition. The measurement uncertainty of the Nusselt number is about  $\pm 8.0\%$ , and the temperature measurement uncertainty is about  $\pm 0.2^{\circ}\text{C}$ .

#### 4. Conclusions

In the first part of the paper, a systematic introduction to the thermochromic liquid crystal (TLC) and the liquid crystal thermography has been presented. Based on the literature review and our experiences in the use of the TLC for the heat transfer measurements, the liquid crystal thermography calibration procedures have been detailedly described, and the parameters, which can influence the TLC temperature measurement uncertainty, have been investigated. The study shows that the use of an image noise reduction technique, the TLC coating thickness, the lighting angle, and the coating quality can distinctively influence the TLC hue calibration and the temperature measurement uncertainty. In the second part of the paper, examples of the applications of the steady and transient liquid crystal thermography techniques to the turbulent convective heat transfer measurements have been introduced.

## Acknowledgment

The research work was funded by the National Natural Science Foundation of China (Funding nos. 51176111 and 5806045).

## References

- [1] Hallcrest, *Handbook of Thermochromic Liquid Crystal Technology*, 1991.
- [2] Y. Rao and S. Zang, "Calibrations and the measurement uncertainty of wide-band liquid crystal thermography," *Measurement Science and Technology*, vol. 21, no. 1, Article ID 015105, 2010.
- [3] P. T. Ireland, A. J. Neely, D. R. H. Gillespie, and A. J. Robertson, "Turbulent heat transfer measurements using liquid crystals," *International Journal of Heat and Fluid Flow*, vol. 20, no. 4, pp. 355–367, 1999.
- [4] P. T. Ireland and T. V. Jones, "Liquid crystal measurements of heat transfer and surface shear stress," *Measurement Science and Technology*, vol. 11, no. 7, pp. 969–986, 2000.
- [5] C. Camci, K. Kim, and S. A. Hippensteele, "A new hue capturing technique for the quantitative interpretation of liquid crystal images used in convective heat transfer studies," *Journal of Turbomachinery*, vol. 114, no. 4, pp. 765–775, 1992.
- [6] D. J. Farina, J. M. Hacker, R. J. Moffat, and J. K. Eaton, "Illuminant invariant calibration of thermochromic liquid crystals," *Experimental Thermal and Fluid Science*, vol. 9, no. 1, pp. 1–12, 1994.
- [7] M. Behle, K. Schulz, W. Leiner, and M. Fiebig, "Color-based image processing to measure local temperature distributions by wide-band liquid crystal thermography," *Applied Scientific Research*, vol. 56, no. 2-3, pp. 113–143, 1996.
- [8] D. R. Sabatino, T. J. Praisner, and C. R. Smith, "A high-accuracy calibration technique for thermochromic liquid crystal temperature measurements," *Experiments in Fluids*, vol. 28, no. 6, pp. 497–505, 2000.
- [9] T. L. Chan, S. Ashforth-Frost, and K. Jambunathan, "Calibrating for viewing angle effect during heat transfer measurements on a curved surface," *International Journal of Heat and Mass Transfer*, vol. 44, no. 12, pp. 2209–2223, 2001.
- [10] T. B. Roth and A. M. Anderson, "The effects of film thickness, light polarization, and light intensity on the light transmission characteristics of thermochromic liquid crystals," *Journal of Heat Transfer*, vol. 129, no. 3, pp. 372–378, 2007.
- [11] R. Wiberg and N. Lior, "Errors in thermochromic liquid crystal thermometry," *Review of Scientific Instruments*, vol. 75, no. 9, pp. 2985–2994, 2004.
- [12] N. Abdullah, A. R. A. Talib, H. R. M. Saiah, A. A. Jaafar, and M. A. M. Salleh, "Film thickness effects on calibrations of a narrowband thermochromic liquid crystal," *Experimental Thermal and Fluid Science*, vol. 33, no. 4, pp. 561–578, 2009.
- [13] Y. Rao, S. Zang, and C. Wan, "Effect of coating thickness on the calibration and measurement uncertainty of a wide-band liquid crystal thermography," *Chinese Optics Letters*, vol. 8, no. 4, pp. 395–397, 2010.
- [14] MATLAB 2007 R2007a help document, The MathWorks Inc.
- [15] M. Maurer, J. von Wolfersdorf, and M. Gritsch, "An experimental and numerical study of heat transfer and pressure loss in a rectangular channel with V-shaped ribs," *Journal of Turbomachinery*, vol. 129, no. 4, pp. 800–808, 2007.
- [16] Y. Rao, C. Wan, Y. Xu, and S. Zang, "Local heat transfer characteristics in channels with pin fin and pin fin-dimple arrays," in *Proceedings of the ASME of Turbine Technical Conference and Exposition (GT '11)*, 2011.
- [17] Y. Rao, C. Wan, Y. Xu, and S. Zang, "Spatially-resolved heat transfer characteristics in channels with pin fin and pin fin-dimple arrays," *International Journal of Thermal Sciences*, vol. 50, no. 11, pp. 2277–2289, 2011.
- [18] S. C. Jenkins, I. V. Shevchuk, J. von Wolfersdorf, and B. Weigand, "Transient thermal field measurements in a high aspect ratio channel related to transient thermochromic liquid crystal experiments," *Journal of Turbomachinery*, vol. 134, Article ID 031002, 10 pages, 2012.
- [19] S. V. Ekkad and J. C. Han, "A transient liquid crystal thermography technique for gas turbine heat transfer measurements," *Measurement Science and Technology*, vol. 11, no. 7, pp. 957–968, 2000.
- [20] M. Schüler, S. O. Neumann, and B. Weigand, "Experimental investigations of pressure loss and heat transfer in a 180° bend of a ribbed two-pass internal cooling channel with engine-similar cross-sections," *Journal of Power and Energy A*, vol. 223, no. 6, pp. 709–719, 2009.

## Research Article

# Applying a Self-Made Automobile Heterodyne Interferometer to Measure the Parameters of Twisted Nematic Liquid Crystal

Shinn-Fwu Wang, Pei-Cheng Ke, Wesley Lai, Hao Ma, Yi-Zhan Su, and Jyh-Shyan Chiu

Department of Electronic Engineering, Chien Hsin University of Science and Technology, No. 229 Chien-Hsin Road, Taoyuan, Zhongli City 320, Taiwan

Correspondence should be addressed to Shinn-Fwu Wang, sfwangking@gmail.com

Received 13 July 2012; Revised 28 September 2012; Accepted 5 October 2012

Academic Editor: Ashish K. Prajapati

Copyright © 2012 Shinn-Fwu Wang et al. This is an open access article distributed under the Creative Commons Attribution License, which permits unrestricted use, distribution, and reproduction in any medium, provided the original work is properly cited.

A self-made automobile heterodyne interferometer with a closed control loop is presented. In addition, we will apply the self-made automobile heterodyne interferometer to measure the parameters of optically compensated twisted nematic liquid crystal (TN LC). It is worthy to be mentioned that the self-made automobile heterodyne interferometer has a compact size because all the optical components are installed in the mechanism of the system. Besides, the self-made automobile heterodyne interferometer has some much more merits, for example, automobile control, a simple setup, in real-time test, reliability, and so forth. Besides, it is very stable because of its common optical path insensitive to environmental disturbances. And its feasibility is demonstrated.

## 1. Introduction

As is well known, liquid crystal displays (LCDs) have several distinct advantages, for example, light weight, thin and less volume over the conventional displays. In recent years, it has grown rapidly and been applied in many products, such as pads, smart mobile phone screen, notebook panel, PC screen, and LCD TV. If large LCDs are used for monitor and TV applications, they must be with the performance of wide-viewing angle. Because of the optically compensated twisted nematic liquid crystal with the characteristics of fast response and wide viewing angle [1, 2], it has been used in large size LCDs for monitor and TV applications.

In fact, it is necessary for us to inspect the quality of OCB based on the importance of OCB with fast response and wide viewing angle. Many articles [3–6] that have been proposed to measure the cell parameters have been based on intensity detection by a photometric technique and developed relations between measured intensity and cell parameters recently. Tseng et al. presented a measuring technique [7] to determine the twist angle, pretilt angle, and cell gap of a TN LC cell based on the phase-sensitive heterodyne interferometry. Because of the measuring technique with buck optical components, Wang et al. proposed a new measuring method

[8] by phase-sensitive heterodyne interferometry to measure phase retardation versus rotational angle of an OCB cell and determine the cell parameters by curving fittings to theoretical calculations in 2010.

In this paper, we propose a self-made automobile heterodyne interferometer with a closed control loop. Although the experimental scheme is similar to some previous articles [7, 8] on phase-sensitive heterodyne interferometry, the interferometer is to be designed as the vertical type with easy operation and test. It is worthy to be mentioned that the interferometer has a compact size because all the optical components are installed in the mechanism of the system. Besides, the interferometer has some much more merits, for example, automobile control, a simple setup, in real-time test, reliability, and so forth.

## 2. Principles

**2.1. A Heterodyne Optical Source.** In this paper, a heterodyne light [9] with a 2 KHz beat frequency will be used. As shown in Figure 1, the optical structure of the heterodyne light is composed of a laser diode with the wavelength of 635 nm, laser diode driver circuits, collimating lens, a polarizer

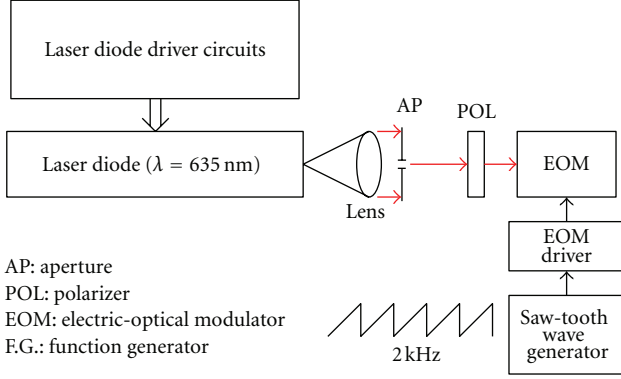


FIGURE 1: A heterodyne optical source with a 2 KHz beat frequency.

(POL), an aperture (AP), an EOM, an EOM driver, and a saw-tooth wave generator. The EOM is modulated by driving a saw-tooth wave with the frequency of 2 KHz. For the sake of compact size, we design a saw-tooth wave generator consisting of IC TL082 and some electronic components instead of a function generator (FG).

**2.2. The Driving Circuits of Step Motor and 5-Axis Machine Arm.** At this time, let us introduce the driving circuits of step motor and 5-axis machine arm of the self-made automobile heterodyne interferometer. In the interferometer, we design a platform, that is, rotation stage, on which the tested LC can be placed. In order to rotate the platform by a step motor, the platform is designed as a round shape with 200 gears. Figure 2 shows the 3-D structure of the platform driven by a step motor.

In the paper, a 4-phase step motor is used to drive the platform. In fact, it is necessary for us to provide a large enough driving current to push any one phase of the step motor. Figure 3 shows the driving circuits with a darling pair to drive one phase of the step motor.

In order to fetch the tested LC, a five-axis machine arm (see Figure 4(a)) manufactured by I-Chung Computer Co. Lt'd in Taiwan is used. The five-axis machine arm is with five axes including wrist, shoulder, finger, elbow, and base. Every arm can undergo either up (close) or down (open) by sending digital signals to the inputs of the arm's driving circuits composed of two photo-couplers shown in Figure 4(b). If we send 1 (or V(1)) to the photocoupler INA1 and 0 (or V(0)) to the photocoupler INA2, respectively; thus INA1 will turn on and INA2 will turn off. At this moment, the machine arm A will be up, and vice versa.

**2.3. The Principles of Optically Compensated Twisted Nematic Liquid Crystal.** In this paper, we try to measure the parameters of a twisted nematic liquid crystal by using the self-made automobile heterodyne interferometer. It is important for us to understand the principles of optically compensated twisted nematic liquid crystals at this time. In this paper, we want to measure the phase retardation of an optically compensated nematic liquid crystal display panel. For convenience, the liquid crystal cell is equally divided into  $m$  thin

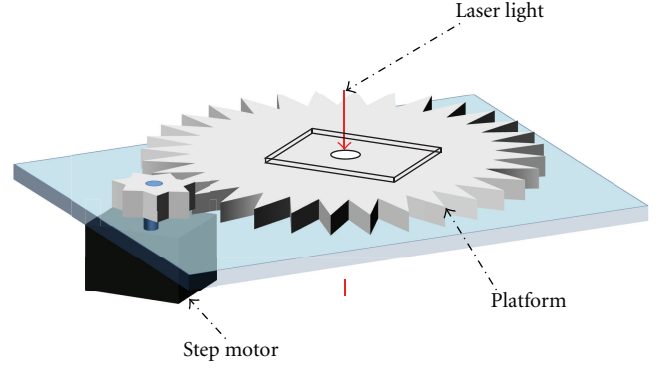


FIGURE 2: The 3-D structure of the platform driven by a step motor.

layers. In addition, each layer can be approximately regarded as a uniaxial wave plate if  $m$  is large enough. According to the Jones matrix method, the electric field of the laser beam that passes the cell can be evaluated by multiplying all the matrixes associated with each layer in sequence as given by the following equation [8]:

$$\begin{aligned}
 \begin{bmatrix} E_x \\ E_y \end{bmatrix} &= \begin{bmatrix} 0 & 0 \\ 0 & 1 \end{bmatrix} R(-\theta_r - 90) \begin{bmatrix} e^{in_e \cdot 2\pi/\lambda \cdot d/m} & 0 \\ 0 & e^{in_o \cdot 2\pi/\lambda \cdot d/m} \end{bmatrix} \\
 &\times R\left(\frac{90}{m}\right) \cdots R\left(\frac{90}{m}\right) \begin{bmatrix} e^{in_e \cdot 2\pi/\lambda \cdot d/m} & 0 \\ 0 & e^{in_o \cdot 2\pi/\lambda \cdot d/m} \end{bmatrix} \\
 &\times R\left(\frac{90}{m}\right) \begin{bmatrix} e^{in_e \cdot 2\pi/\lambda \cdot d/m} & 0 \\ 0 & e^{in_o \cdot 2\pi/\lambda \cdot d/m} \end{bmatrix} \\
 &\times R(\theta_r) \begin{bmatrix} \cos \frac{\Gamma}{2} \\ i \sin \frac{\Gamma}{2} \end{bmatrix}, \\
 \begin{bmatrix} E_x \\ E_y \end{bmatrix} &\equiv \begin{bmatrix} 0 & 0 \\ p + iq & r + is \end{bmatrix} \begin{bmatrix} \cos \frac{\Gamma}{2} \\ i \sin \frac{\Gamma}{2} \end{bmatrix}, \tag{1}
 \end{aligned}$$

where  $\Gamma$  is the phase introduced by the EOM,  $\theta_r$  is the initial azimuth angle of the rubbing direction of the cell,  $R$  is the coordinate rotation matrix,  $n_o$  and  $n_e$  are the refraction indices of the ordinary and extraordinary waves, respectively,  $d$  is the cell gap, and  $\lambda$  is the wavelength of the laser diode. As the electric field of the transmitted laser beam is determined, the intensity can be express as

$$\begin{aligned}
 I &\equiv |E|^2 = E_x^2 + E_y^2, \\
 I &\equiv C + \sqrt{A^2 + B^2} \cos(\Gamma + \phi), \tag{2}
 \end{aligned}$$

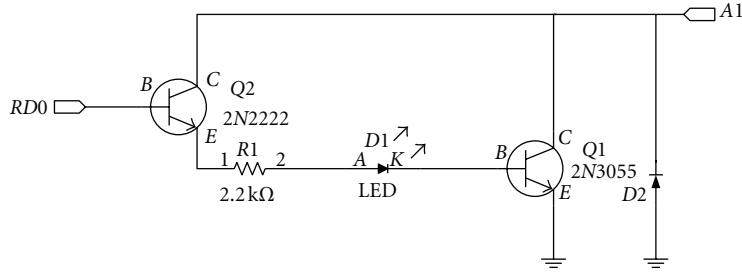


FIGURE 3: The driving circuits with a Darlington pair to drive one phase of the step motor.

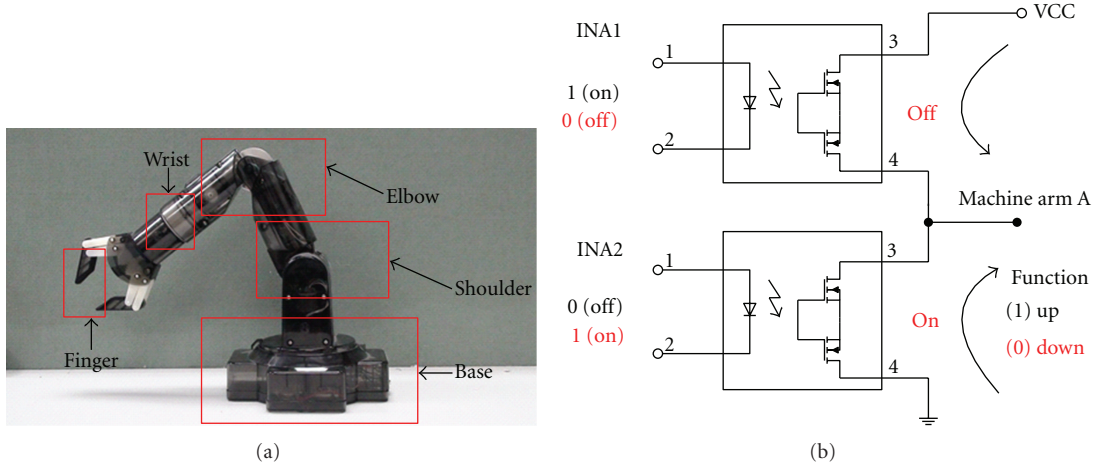


FIGURE 4: (a) A five-axis machine arm manufactured by I-Chung Computer Co. Ltd. (b) The machine arm's driving circuits composed of two photo-couplers.

where

$$\begin{aligned}
 A &= \frac{1}{2}(r^2 + s^2 - p^2 - q^2), \\
 B &= qr - ps, \\
 C &= \frac{1}{2}(p^2 + q^2 + r^2 + s^2), \\
 \phi &= \tan^{-1} \frac{B}{A}; \quad -\pi < \phi < \pi.
 \end{aligned}
 \tag{3}$$

Thus we obtain the theoretical phase retardation,  $\phi$ , of the optically compensated twisted nematic LC cell.

### 3. Experimental Apparatus

The experimental setup of the interferometer is shown in Figure 5. In the experimental configuration, a heterodyne light with a beat frequency  $f = 2$  KHz passes through the tested optically compensated twisted nematic LC and an analyzer AN and then enters a photodetector PD. The signal measured by PD is the test signal. Besides, we can obtain the reference signal from the saw-tooth wave generator. These two signals are sent to a lock-in amplifier (LIA NI USB-4431 manufactured by National Instruments, USA) with the resolution  $\Delta\Phi$  of  $0.01^\circ$ . Thus, we can obtain the phase retardation versus rotational angle of optically compensated

twisted nematic LC cell. After some numerical computations by a computer, the cell parameters will be determined by curving fittings.

Figure 6 shows the 3-D structure of the self-made automobile heterodyne interferometer. And the photo picture of the interferometer is shown in Figure 7.

### 4. Results

In this paper, we try to measure the parameters of optically compensated twisted nematic liquid crystal (TN LC) by using the self-made automobile heterodyne interferometer. The flow chart of its program is depicted in Figure 8. As some TN LCs are prepared to be tested, the system must initialize at first. Then personal computer (PC) sends the control instruction to order the machine arm to pick up the tested LC that is placed on the unfinished region. Afterwards, the machine arm picks up the tested LC and moves it to the platform. And that the machine arm puts the tested LC on the platform, and the system begins to measure the LC. After the test has finished, the machine arm picks up the tested LC and moves it to the finished region. The system will undergo the measurement of another LC again until all of the LCs are tested completely.

In this paper, we try to measure a piece of optically compensated TN LC provided by the Research and Development Center, HannStar Display Corporation. The corresponding

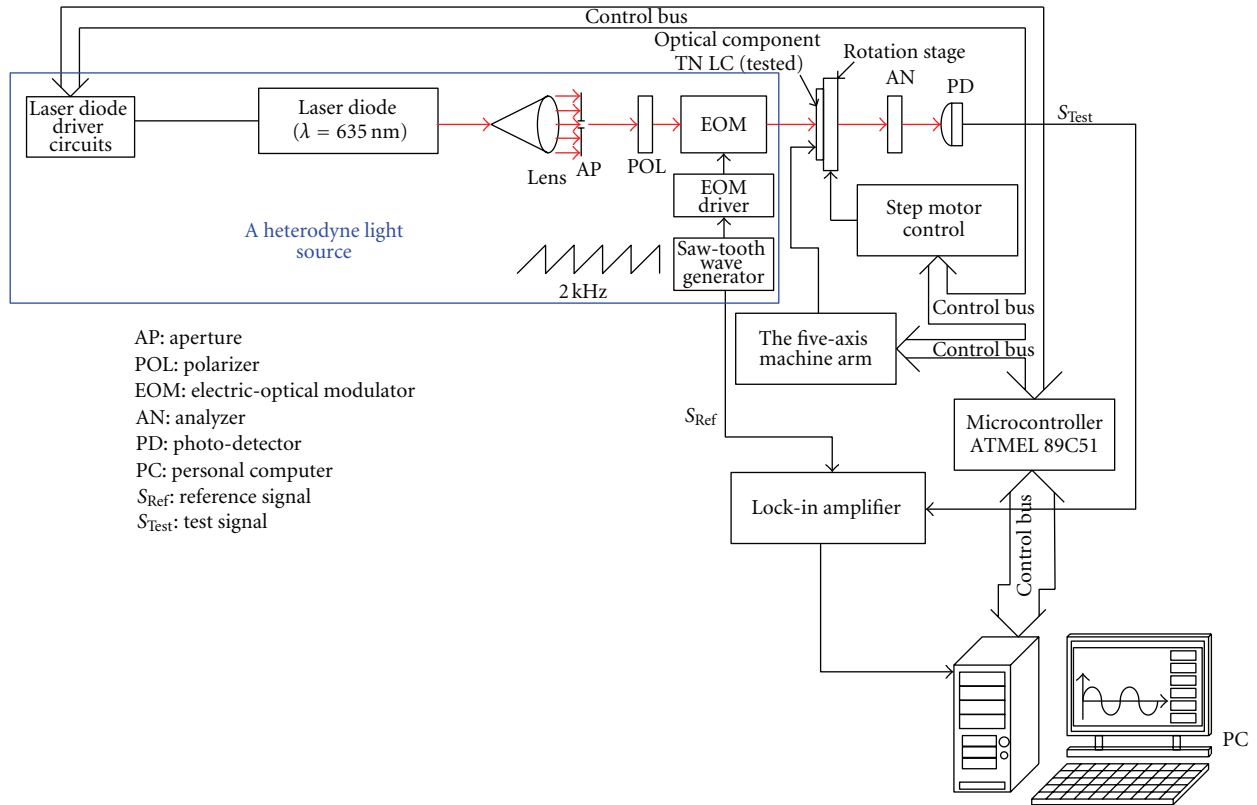


FIGURE 5: The experimental setup of the self-made automobile heterodyne interferometer.

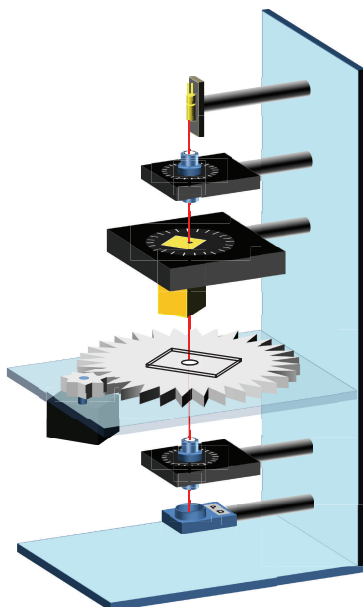


FIGURE 6: The 3-D structure of the self-made automobile heterodyne interferometer.

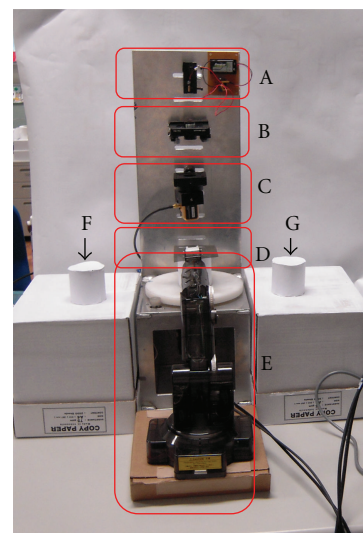


FIGURE 7: The photo picture of the self-made automobile heterodyne interferometer (A: laser diode driving circuits; B: laser diode with the wavelength of 635 nm; C: EOM, electrooptical modulator; D: the tested LC; E: five-axis machine arm; F: the unfinished region; G: the finished region).

LC cell parameters such as, cell gap, pretilt angle, extraordinary refractive index, and ordinary refractive index are  $3.7 \mu\text{m}$ , 6.044 degree,  $n_e = 1.574$ , and  $n_o = 1.476$ , respectively. In this paper, we apply the heterodyne interferometer

to measure the phase retardation versus rotational angle of an optically compensated TN LC cell.

As a matter of fact, we can measure the pretilt angle and cell gap of a TN LC cell by using the heterodyne

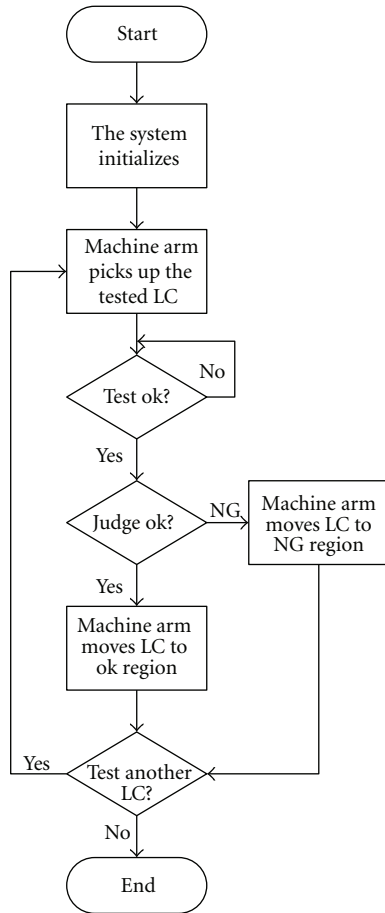


FIGURE 8: The flow chart of the control program.

interferometer. To obtain the cell parameters, we carry out a fitting procedure based on comparing the experimentally measured data with the theoretically calculated values by using iterative calculations. The experimental data and fitting curve are shown in Figure 9. From the results, the corresponding cell parameters of the optically compensated TN LC such as cell gap and pretilt angle, are determined to have  $3.68 \mu\text{m}$  and  $6.01$  degree, respectively. The data are in agreement with that of the manufacturer (cell gap equal to  $3.7 \mu\text{m}$  and pretilt angle equal to  $6.044$  degree).

## 5. Discussions and Conclusion

In the paper, a self-made automobile heterodyne interferometer with a closed control loop is proposed. However, the setup of the interferometer for measuring the phase retardation is compact, easy to operate, in real-time measurement, and simple. Besides, it is very stable because of its common optical path insensitive to environmental disturbances. In the interferometer, we design a control circuits with a closed loop by using the serial communication between the PC and MCS-51 controller. Besides, we can design an automobile precision measurement system by combining the heterodyne interferometer and some small displacement sensor [10] or small angle sensor [11]. In conclusion, we must state that

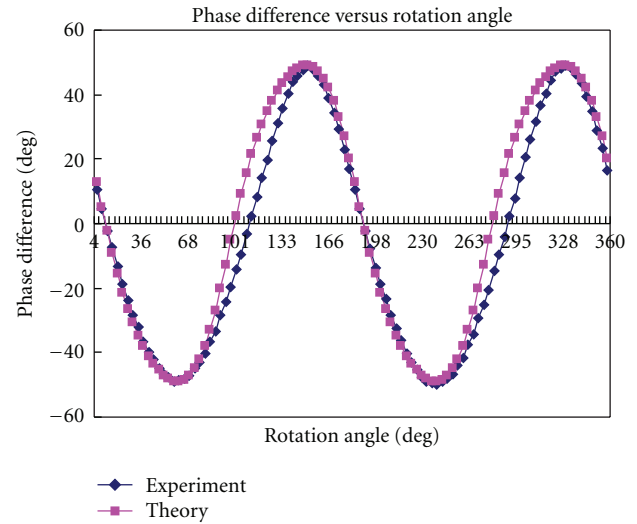


FIGURE 9: The experimental and theoretical data.

the heterodyne interferometer is original and valuable for integrated circuits (IC) industry, electrooptical industry, precision industry, and so forth. And its feasibility is demonstrated.

## Acknowledgments

This research was partially supported by the National Science Council in Taiwan through Grant NSC 100-2632-E-231-001-MY3 and partially supported by the Research and Development Center, HannStar Display Corporation.

## References

- [1] Y. Yamaguchi, T. Miyashita, and T. Uchida, in *Proceedings of the Society for Information Display (SID '93)*, p. 277, 1993.
- [2] P. J. Boss and J. A. Rahman, in *Proceedings of the Society for Information Display (SID '93)*, p. 273, 1993.
- [3] J. A. Davis, I. Moreno, and P. Tsai, "Polarization eigenstates for twisted-nematic liquid-crystal displays," *Applied Optics*, vol. 37, no. 5, pp. 937–945, 1998.
- [4] Y. Zhou, Z. He, and S. Sato, "A novel method for determining the cell thickness and twist angle of a twisted nematic cell by stokes parameter measurement," *Japanese Journal of Applied Physics*, vol. 36, pp. 2760–2764, 1997.
- [5] H. Kim and Y. H. Lee, "Unique measurement of the parameters of a twisted-nematic liquid-crystal display," *Applied Optics*, vol. 44, no. 9, pp. 1642–1649, 2005.
- [6] J. S. Gwag, S. H. Lee, K. H. Park et al., "Simple method for measuring the high pretilt angle of nematic liquid crystals," *Journal of Applied Physics*, vol. 93, no. 8, pp. 4936–4938, 2003.
- [7] H.-C. Tseng, R. B. Li, W.-C. Chen, K. H. Yang, and S.-F. Wang, "Determinations of twist angle, pretilt angle, and cell gap of a TN LC cell by phase-sensitive heterodyne interferometry," in *Proceedings of the Society for Information Display (SID '08)*, Los Angeles Convention Center, Los Angeles, Calif, USA, May 2008.
- [8] S.-F. Wang, W. Lai, J.-S. Chiu, R. H. Yeh, H.-C. Tseng, and W.-C. Chen, "Method for measuring the twist angle of an optically compensation bend by using the heterodyne interferometry,"

- in *Proceedings of the IEEE International Instrumentation and Measurement Technology Conference (I2MTC '10)*, pp. 296–299, 2010.
- [9] M. H. Chiu, S.-F. Wang, and R. S. Chang, “Instrument for measuring small angles by use of multiple total internal reflections in heterodyne interferometry,” *Applied Optics*, vol. 43, no. 29, pp. 5438–5442, 2004.
  - [10] S.-F. Wang, “A small-displacement sensor using total internal reflection theory and surface plasmon resonance technology for heterodyne interferometry,” *Sensors*, vol. 9, pp. 2498–2510, 2009.
  - [11] S.-F. Wang, M. H. Chiu, C. W. Lai, and R. S. Chang, “High-sensitivity small-angle sensor based on surface plasmon resonance technology and heterodyne interferometry,” *Applied Optics*, vol. 45, no. 26, pp. 6702–6707, 2006.